




Turun yliopisto  
University of Turku

A large, stylized green graphic on the left side of the cover. It consists of a central vertical stem that branches out into a series of curved, fan-like segments, resembling a shell or a stylized plant. The segments are arranged in a semi-circular pattern, creating a sense of depth and movement.

# PRASEODYMIUM CALCIUM MANGANITES: MAGNETISM ACROSS LENGTH SCALES

Jussi Tikkanen



Turun yliopisto  
University of Turku

# PRASEODYMIUM CALCIUM MANGANITES: MAGNETISM ACROSS LENGTH SCALES

---

Jussi Tikkanen

## University of Turku

---

Faculty of Mathematics and Natural Sciences  
Department of Physics and Astronomy  
From the Wihuri Physical Laboratory

## Supervised by

---

Prof. Petriina Paturi  
Wihuri Physical Laboratory  
Dept. of Physics and Astronomy  
University of Turku  
Turku, Finland

Dr. Hannu Huhtinen  
Wihuri Physical Laboratory  
Dept. of Physics and Astronomy  
University of Turku  
Turku, Finland

## Reviewed by

---

Doc. Johan Lindén  
Physics Department  
Åbo Akademi  
Turku, Finland

Dr. Christian Bahl  
Dept. of Energy Conversion and Storage  
Technical University of Denmark  
Roskilde, Denmark

## Opponent

---

Prof. Roland Mathieu  
Dept. of Engineering Sciences  
Uppsala University  
Uppsala, Sweden

The originality of this thesis has been checked in accordance with the University of Turku quality assurance system using the Turnitin OriginalityCheck service.

ISBN 978-951-29-6872-5 (PRINT)

ISBN 978-951-29-6873-2 (PDF)

ISSN 0082-7002 (Print)

ISSN 2343-3175 (Online)

Painosalama Oy - Turku, Finland 2017

# Preface

## Acknowledgments

This work has been carried out in the Wihuri Physical Laboratory of the Department of Physics and Astronomy at the University of Turku. The Jenny and Antti Wihuri Foundation and the University of Turku Graduate School's Doctoral Programme in Physical and Chemical Sciences are acknowledged for their generous financial support. I'm very thankful to Doc. Johan Lindén and Dr. Christian Bahl for all of their time and their insightful reviews of this dissertation. I also wish to specially thank Prof. Roland Mathieu, it is a great honor to have you as my opponent.

For her supervision, personal trust and constant commitment to the whole group, Prof. Petriina Paturi has also earned my deepest gratitude, as has Dr. Hannu Huhtinen, who masterfully taught me how to stop worrying and keep the equipment running. Though it turns out to be impossible to pin the blame for the uniquely supportive atmosphere of the Wihuri Physical Laboratory on any individual, among all of my esteemed colleagues, I will certainly never forget how MSc Mika Malmivirta has always been within earshot, able to hear out any problem I might come up with, and more often than not solve it with a limping joke delivered at surgical precision. My special thanks also go to our collaborators overseas – Dr. Jean-Claude Grivel for teaching me the work ethics of a true synthetist, Prof. Linda Udby for introducing me to the world of neutrons, and the former and present members of the Halle group, in particular Prof. Wolfram Hergert and Dr. Matthias Geilhufe, for helping me finally make some theoretical sense out of everything.

Certainly enough, none of this work would have been possible without the ever-reliable support of my family and friends. All the relaxing hours, expeditions and cold pints in good company have gone a long way to keep me in my senses. Especially Justiina has deserved all the credit I can give her for helping me keep my priorities straight. Thank you.

Turku, May 2017

*Jussi Tikkanen*

## Abstract

In this work, the methods of experimental and computational material physics are employed to describe and explain the magnetic phase diagram of  $\text{Pr}_{1-x}\text{Ca}_x\text{MnO}_3$ , a particular family of perovskite-structured manganites (hereafter PCMO) perhaps most famous for its prominent colossal magnetoresistivity effect. After introducing the basic structural and magnetic properties of perovskite manganites and finally the macroscopic magnetic phase diagram of PCMO, the microscopic mechanisms at the origin of the directly observable macroscopic phases of PCMO are identified and modeled.

The experimental research was largely based on ceramic samples synthesized by the traditional solid state method. The highly crystalline samples were readily characterized by diffractometric methods, including x-ray and neutron diffraction assisted by Rietveld refinement, and bulk magnetometry down to the liquid helium temperature. Thus, experimental correlations between the structural and magnetic properties of PCMO could be established. Structural problems only arose at the highest of Ca concentrations, at  $x \geq 0.8$ , where a structural phase separation and a thermodynamic preference for severe oxygen understoichiometry were verified.

At  $x \leq 0.8$ , a consistent description of the magnetic phase diagram was achieved based on a microscopic dynamic equilibrium between only two magnetic phases, significantly extending the range of applicability of such a framework for PCMO. The phase equilibrium was characterized via several distinct observations of structural transitions and exotic magnetization dynamics, and finally modeled by Monte Carlo simulations capable of reproducing the magnetic hysteresis of PCMO, including the metamagnetic transition related to the colossal magnetoresistance effect. As a natural byproduct of analyzing the magnetic transitions, entropy-based estimates for the magnetocaloric applicability of PCMO were also obtained. The estimated refrigerant capacities placed the 100 K performance of PCMO on par with the room temperature figures of some of the best Gd-based magnetocaloric alloys.

## Tiivistelmä

Tässä työssä sovellettiin kokeellisen ja laskennallisen materiaalfysiikan menetelmiä perovskiittirakenteisen manganiittiperhe  $\text{Pr}_{1-x}\text{Ca}_x\text{MnO}_3$ :n (jäljempänä PCMO) magneettisen faasidiagrammin selvittämiseksi. Materiaaliryhmä on kenties kuuluisin ns. kolossaalisesta magnetoiresistiivisyysilmiöstään. Perovskiittimanganiittien rakenteellisten ja magneettisten perusominaisuuksien esittelyn jälkeen työssä kuvaillaan PCMO:n makroskooppinen magneettinen faasidiagrammi, joka pyritään lopulta ymmärtämään suoraan havaittavissa olevien makroskooppisten faasien taustalla vaikuttavien mikroskooppisten mekanismien kautta.

Tutkimustyön kokeellinen osa perustui pitkälti perinteisellä kiinteän olomuodon menetelmällä tuotettuihin keraamisiin näytteisiin, joiden ominaisuudet voitiin määrittää suoraviivaisesti diffraktometrisin menetelmin, kuten Rietveld-avusteisella röntgen- ja neutronidiffraktiolla, sekä magnetometrisesti aina nestemäisen heliumin lämpötilaan saakka. Näin saatiin kokeellisesti todennettua korrelaatioita PCMO:n rakenteellisten ja magneettisten ominaisuuksien välillä. Rakenteellisiä ongelmia ilmeni vain korkeimmilla Ca-konsentraatioilla,  $x \geq 0.8$ , joilla havaittiin kiderakenteen faasiseparaatio ja termodynaaminen taipumus huomattavaan alistoikiometriaan hapen suhteen.

Alueella  $x \leq 0.8$  magneettisesta faasidiagrammista saatiin laadittua sisäisesti harmoninen malli, joka perustui mikroskooppiseen dynaamiseen tasapainoon vain kahden magneettisen faasin välillä. Näin faasiseparaatioviitekehyksen sovellusala PCMO:n kuvauksessa saatiin laajennettua huomattavasti. Tasapainomekanismia opittiin ymmärtämään useiden erillisten rakenteellisiin transiitioihin ja eksoottiseen magnetisaatiodynamiikkaan viittaavien havaintojen kautta, ja mekanismi kyettiin viimein mallintamaan Monte Carlo -simulaatioilla, jotka toistivat PCMO:n magneettisen hystereesin kolossaaliseen magnetoiresistanssi-ilmiöön liittyvää metamagneettista transiitiota myöten. Luonnollisena sivujuonteena magneettisten transiitoiden analyysin pohjalta laadittiin myös entropiamuutoksiin perustuva arvio PCMO:n magnetokalorisesta hyödynnettävyydestä, joka osoittautui n. 100 K:n lämpötilassa yhtä hyväksi kuin eräiden parhaiden Gd-pohjaisten magnetokaloristen lejeerinkien ennuste huoneenlämpötilassa.

## Articles included in this thesis

This thesis is based on work carried out at the Wihuri Physical Laboratory, Department of Physics and Astronomy, University of Turku during the years 2013–2017. The thesis consists of an introductory part and the following publications:

- [P1] J. Tikkanen, H. Huhtinen and P. Paturi: *Oxygen-sintered (Pr,Ca)MnO<sub>3</sub>: Structure and magnetism at high Ca concentrations*, J. Alloys Compd. **635** (2015) 41–47, doi:10.1016/j.jallcom.2015.02.098
- [P2] J. Tikkanen, S. Kauhala, H. Huhtinen and P. Paturi: *Anomalous Thermal Expansion in (Pr,Ca)MnO<sub>3</sub> due to Orbital Ordering*, Phys. Procedia **75** (2015) 475–481, doi:10.1016/j.phpro.2015.12.059
- [P3] J. Tikkanen, H. Huhtinen and P. Paturi: *The Magnetocaloric Performance of (Pr,Ca) Manganites Estimated by Magnetic Transition Entropies*, IEEE Trans. Magn. **50** (2014) 2504004, doi:10.1109/TMAG.2014.2324656
- [P4] J. Tikkanen, M. Geilhufe, M. Frontzek, W. Hergert, A. Ernst, P. Paturi and L. Udby: *The low-temperature magnetostructure and magnetic field response of Pr<sub>0.9</sub>Ca<sub>0.1</sub>MnO<sub>3</sub>: the roles of Pr spins and magnetic phase separation*, J. Phys.: Cond. Matter **28** (2016) 036001, doi:10.1088/0953-8984/28/3/036001
- [P5] J. Tikkanen, H. Huhtinen and P. Paturi: *A dynamic mesoscale model of the metamagnetic transition in low bandwidth perovskite manganites* (submitted)

## Articles relevant to this work but not included in the thesis

- [P6] A. Beiranvand, J. Tikkanen, J. Rautakoski, H. Huhtinen and P. Paturi: *Estimates of the magnetocaloric effect in (Nd,Ca)MnO<sub>3</sub> and (Gd,Ca)MnO<sub>3</sub> based on magnetic transition entropies*, Materials Research Express **4** (2017) 036101, url:<http://stacks.iop.org/2053-1591/4/i=3/a=036101>
- [P7] P. Paturi, J. Tikkanen and H. Huhtinen: *Room temperature charge-ordered phase in Gd<sub>0.6</sub>Ca<sub>0.4</sub>MnO<sub>3</sub> and Sm<sub>0.6</sub>Ca<sub>0.4</sub>MnO<sub>3</sub> thin films*, J. Magn. Magn. Mater. **432** (2017) 164–168, doi:10.1016/j.jmmm.2017.01.080

- [P8] I. Angervo, M. Saloaro, J. Tikkanen, H. Huhtinen and P. Paturi: *Improving the surface structure of high quality  $Sr_2FeMoO_6$  thin films for multilayer structures*, Appl. Surf. Sci. **396** (2017) 754–759, doi :10.1016/j.apsusc.2016.11.021
- [P9] M. Malmivirta, H. Palonen, S. Inkinen, L.D. Yao, J. Tikkanen, H. Huhtinen, R. Jha, V.P. Awana, S. van Dijken and P. Paturi: *Dirty limit scattering behind the decreased anisotropy of doped  $YBa_2Cu_3O_{7-\delta}$  thin films*, J. Phys.: Cond. Matter **28** (2016) 175702, doi :10.1088/0953-8984/28/17/175702
- [P10] M. Nyman, T. Elovaara, J. Tikkanen, S. Majumdar, H. Huhtinen and P. Paturi: *Epitaxially textured  $Pr_{0.6}Ca_{0.4}MnO_3$  Thin Films Under Considerably Low Substrate Temperature*, Phys. Procedia **75** (2015) 1122–1132, doi :10.1016/j.phpro.2015.12.180
- [P11] J. Tikkanen and P. Paturi: *Iron oxide nanocomposite magnets produced by partial reduction of strontium hexaferrite*, EPJ Web of Conferences **74** (2014) 2101–6275, doi :10.1051/epjconf/20147504007



# Contents

<b>Preface</b>	<b>iii</b>
Acknowledgments . . . . .	iii
Abstract . . . . .	iv
Articles included in this thesis . . . . .	vi
<b>1 Introduction</b>	<b>1</b>
1.1 Motivation . . . . .	1
1.2 The perovskite manganite structure . . . . .	2
<b>2 Magnetism of manganites</b>	<b>7</b>
2.1 Magnetic exchange interactions . . . . .	7
2.2 The magnetic phases of manganites . . . . .	11
2.3 The magnetocaloric effect . . . . .	16
<b>3 Experimental details</b>	<b>19</b>
3.1 Sample preparation . . . . .	19
3.1.1 Microcrystalline samples: Ceramic solid state synthesis . . . . .	19
3.1.2 Nanocrystalline samples: Citrate gel autocombustion . . . . .	20
3.2 Sample characterization . . . . .	22
3.2.1 Powder diffractometry . . . . .	22
3.2.2 Rietveld refinement . . . . .	24
3.2.3 Bulk magnetometry . . . . .	28
<b>4 Simulations</b>	<b>32</b>
4.1 The Metropolis–Hastings Monte Carlo algorithm . . . . .	32
4.2 The mesoscale model of magnetic phase separation . . . . .	33
<b>5 Summary of results</b>	<b>37</b>
5.1 The macroscopic magnetostructural phase diagram of PCMO . . . . .	37
5.2 The role of dynamic nanoscale phase separation in PCMO . . . . .	48
<b>6 Conclusions</b>	<b>55</b>
<b>References</b>	<b>57</b>

# 1 Introduction

## 1.1 Motivation

This thesis delves into the magnetism and magnetofunctionality of a particular series of oxide materials, the perovskite manganites  $\text{Pr}_{1-x}\text{Ca}_x\text{MnO}_3$  (hereafter abbreviated to PCMO), studied at all of the stoichiometrically accessible Ca concentrations,  $0 \leq x \leq 1$ . Somewhat inconspicuous though catalytically active semiconductors at room temperature [1, 2], the PCMO series really kicks into action when cooled a few tens of degrees below the room temperature. PCMO can be viewed as the archetype of the so called *low bandwidth manganites*, a group famous for exhibiting one of the strongest magnetoresistive phenomena ever observed – the *colossal magnetoresistance* (CMR) effect, which comes into play at temperatures below ca. 250 K [3–8].

The CMR effect is basically an insulator–metal transition (IMT) triggered by the application of an external magnetic field, during which the electrical resistivity of the material can decrease by more than a factor of  $10^7$ . Once the field is removed, a reverse transition will conveniently occur (with some hysteresis), returning the material to the original insulating state [9–11]. Obviously, this kind of behavior would make for a great contactless switch, or a very sensitive magnetic field sensor should a biasing magnetic field be applied to pre-tune the material close to the IMT. Furthermore, thanks to the intricate correlations between the electronic, magnetic and elastic degrees of freedom in the perovskite structure [3, 5–7], the IMT can actually be biased by a plethora of other physical stimuli as well, including optical and x-ray illumination [9, 12, 13], applied electric fields [14] and elastic stresses [15, 16] – the low bandwidth manganites are in fact a prime example of *multifunctional materials*.

Before the low bandwidth manganites can mature into any serious applications, however, a handful of fundamental problems still need to be solved. For instance, the critical magnetic field required to drive the IMT is typically quite high, of the order of 10 T [10, 11, 17], and to see a significant CMR effect, the materials must be cooled down to at least ca. 200 K [18]. For practical uses, it would be desirable to have the CMR effect closer to room temperature, around 300 K, and accessible by magnetic fields that can be generated by permanent magnets, putting the upper limit for the field somewhere around 5 T if an extreme Halbach cylinder design can be used [19], and closer to 2 T in a more

down-to-the-earth scenario [20].

To be able to fine-tune the functional properties of manganites, a thorough theoretical understanding of the involved mechanisms would be a great asset. Unfortunately, this poses yet another problem: despite significant advances in computational physics during the recent years [21–24] [P4], the electron–electron and electron–lattice correlations that very much define the nature of manganites [3, 4] remain difficult to model accurately. For this reason, experimental work continues to lead the way in the field, and therein also lies the motivation behind the present thesis work. The objective of this thesis is to experimentally describe a consistent physical picture of the PCMO family, filling in any gaps of knowledge regarding e.g. the sequence of magnetic transitions and magnetic entropy changes, and having collected such data throughout the compositional range, to look for physical correlations that could be refined into phenomenological models of PCMO, the CMR effect and perhaps manganites in general, to help these wonderfully intricate functional materials meet their potential for real-world applications.

## 1.2 The perovskite manganite structure

A lot of the functionality of perovskite manganites stems directly from the characteristics of their particular crystal structure [3, 4, 25], so this is a natural topic with which to begin their description. The word *perovskite* on its own actually refers to a specific mineral form of calcium titanate,  $\text{CaTiO}_3$ , the crystal structure of which (figure 1) is now known to be shared by several groups of silicates, transition metal oxides and halides, only to name some of the most prominent ones. In fact, it is more than likely that this structure is the most common one found on Earth, as perovskite structured silicates of the form  $(\text{Mg,Fe})\text{SiO}_3$  are thought to occupy approximately 80% of the Earth’s mantle by mass [26]. Emphasizing the significance of the perovskite structure over the namesake mineral itself, we will hereafter adopt a common convention and expand the meaning of *perovskite* to describe all perovskite-structured materials.

The ideal structure of a general perovskite,  $\text{ABX}_3$ , could be described by a cubic unit cell with  $A$  atoms at the corners,  $B$  atoms in the center and  $X$  atoms at the face centers. In this configuration, the  $A$  atoms are coordinated to twelve  $X$  atoms, and the  $B$  atoms are symmetrically surrounded by octahedra of six  $X$  atoms. Very few if any compounds adopt this ideal geometry, however,

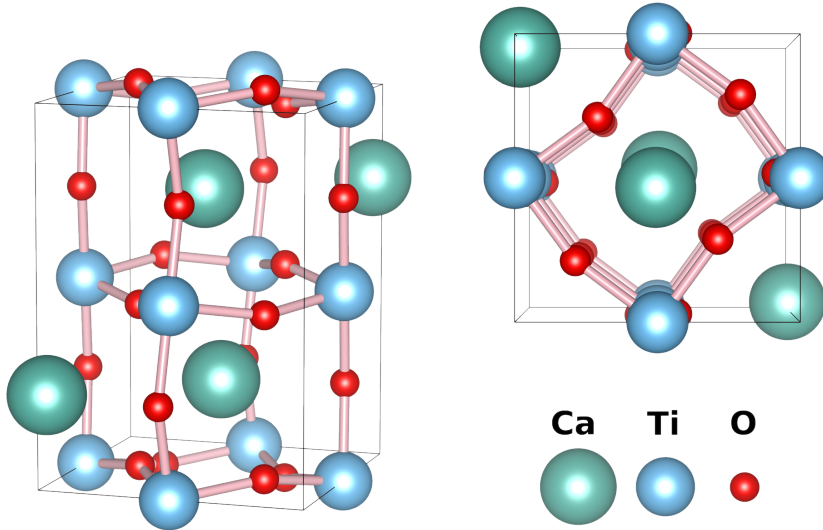


Figure 1. The crystal structure of  $\text{CaTiO}_3$ , also known as perovskite in its mineral form.

and to better appreciate the structural flexibility of perovskite manganites in particular, at least three types of common imperfections, all easily described in terms of the  $X$  octahedra, should be recognized. To help visualize these, the structure is often best drawn with the octahedra made explicitly visible, as in figure 2.

In contrast to the ideal picture, the  $X$  octahedra may actually **(i)** tilt with respect to each other, **(ii)** deform with respect to the central  $B$  atoms<sup>1</sup> and **(iii)** have an  $X$  atom missing. Pure  $\text{CaTiO}_3$  only exhibits **(i)** to any significant extent, so to arrive at a coherent picture of all three imperfections, the rest of this discussion will be specifically in terms of mixed-valence manganites with the general formula  $L_{1-x}M_x\text{Mn}_{1-x+2\delta}^{3+}\text{Mn}_{x-2\delta}^{4+}\text{O}_{3-\delta}^{2-}$ . Here  $L$  is often a lanthanoid element and  $M$  an alkaline earth element, although other similarly sized ions [29] will usually also be compatible with the structure [3]. The  $M$  concentration,  $x$ , is constrained to the interval  $0 \leq x \leq 1$ . Such mixed-valence manganites can be understood as solid solutions between the corresponding parent materials,  $LMnO_3$  and  $MMnO_3$ , complete with the implication that the  $L$  and  $M$  ions are randomly distributed at the  $A$  sites of the mixed structure

<sup>1</sup>For completeness, **(ii)** may also include a small translation, leading to some notable cases of piezo- and ferroelectricity [25, 27, 28].

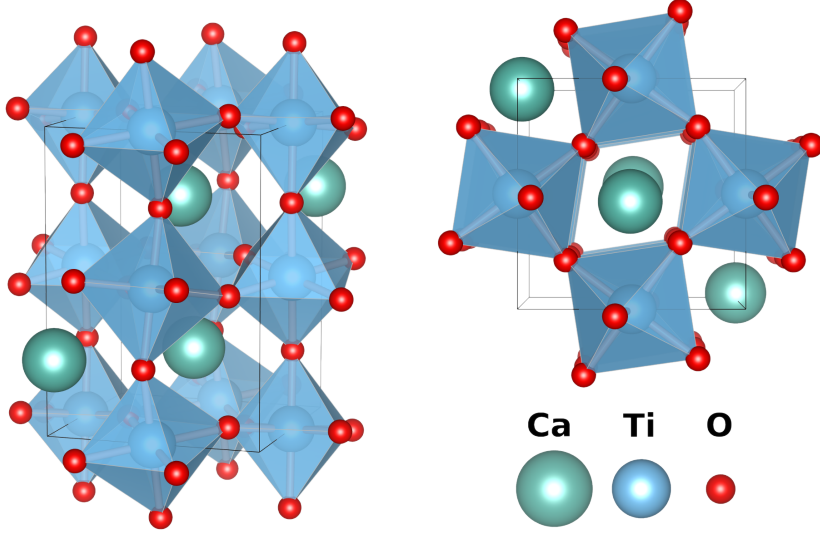


Figure 2. The crystal structure of perovskite,  $\text{CaTiO}_3$ , with the oxygen octahedra made explicitly visible.

[30, 31]. The  $B$  and  $X$  sites, then, are taken by Mn and O, respectively.

In manganites, the geometries of the oxygen octahedra are approximately fixed by their strong interactions (often even covalent bonding [3, 32]) with the outermost occupied electron orbitals of Mn, namely the Mn  $3d$  orbitals [33]. It is therefore reasonable to treat the octahedra as essentially rigid objects which tilt with respect to each other in an attempt to minimize the total electrostatic energy of the configuration [34, 35]. The short explanation for such departures from the ideal, where all Mn–O–Mn bonds would be dead straight, can be given in terms of the effective ionic radii [29] of real world ions, which don't necessarily add up to the bond lengths required for an undistorted perovskite.

This steric "incompatibility" can be quantified by a variety of functionals of the ion size distribution. Perhaps the one most commonly cited is a simple function of the average ionic radii on each crystallographic site called the Goldschmidt tolerance factor [3],  $t$ , defined by

$$t = \frac{\langle r_A \rangle + \langle r_X \rangle}{\sqrt{2}(\langle r_B \rangle + \langle r_X \rangle)}. \quad (1)$$

Here  $\langle r_S \rangle$  denotes the average ionic radius at the site  $S$ . One can verify that the condition  $t = 1$  corresponds to an ideal cubic perovskite. In typical perovskite

manganites,  $t \approx 0.9$ , and below  $t \approx 0.7$  the perovskite structure is typically lost in favor of a rhombohedral one [36].

If each crystallographic site is occupied solely by one corresponding type of ion,  $t$  alone gives a good idea of the steric stress on the perovskite structure. In mixed-valence manganites, however, also the steric disorder caused by the randomness of the  $A$  site ion radius plays a role. This is often described in terms of the variance of the  $A$  site ion radius,  $\sigma^2$ , defined as

$$\sigma^2 = \langle r_A^2 \rangle - \langle r_A \rangle^2 = (x - x^2)(r_L - r_M)^2, \quad (2)$$

where the composition  $L_{1-x}M_x\text{MnO}_{3-\delta}$  is again assumed [36]. Seldom given an absolute interpretation,  $\sigma^2$  more often finds its use in the comparison between mixed-valence manganites of different chemical compositions [31]. An analogous expression with similar applications can be derived for the disorder between  $\text{Mn}^{3+}$  and  $\text{Mn}^{4+}$  ions, which also significantly differ in size [29].

Over sufficiently short timescales and in the absence of external stimuli, the shapes of individual oxygen octahedra can be treated as if they were constant in manganites. However, even in this case, a significant variation of distortions often takes place from octahedron to octahedron, primarily due to the Jahn-Teller (JT) effect [3, 5, 6, 12]. In the octahedral crystal field environment, the five  $3d$  orbitals of Mn form two separate multiplets,  $t_{2g}$  and  $e_g$ , the former of which is always occupied by three electrons in the high spin configuration [37]. In  $\text{Mn}^{4+}$  the  $e_g$  doublet (located roughly 3 eV above the  $t_{2g}$  triplet in energy) is empty, but in  $\text{Mn}^{3+}$  a single electron occupying  $e_g$  renders the ion JT active. This is manifested by a tetragonal distortion of the surrounding octahedron—an elongation along the local  $z$  axis of the octahedron if the symmetry of the occupied  $e_g$  orbital is  $3z^2 - r^2$ , or a compression along  $z$  if the symmetry is  $x^2 - y^2$ . Both symmetries are equally probable *a priori*, since the unoccupied  $e_g$  doublet is degenerate in the absence of environmental perturbations [12].

By the JT mechanism, spatial fluctuations in the Mn valence instantly [12] translate into local distortions in the crystal lattice. Such an effect can greatly compound to the steric distortions discussed above, critically modifying Mn–O–Mn bond angles and thereby the corresponding orbital overlap integrals. The significance of this to the magnetism of manganites will be elaborated on in the following subsections, but in short, the Mn–O–Mn bond angle is the single most important structural parameter determining the magnetic proper-

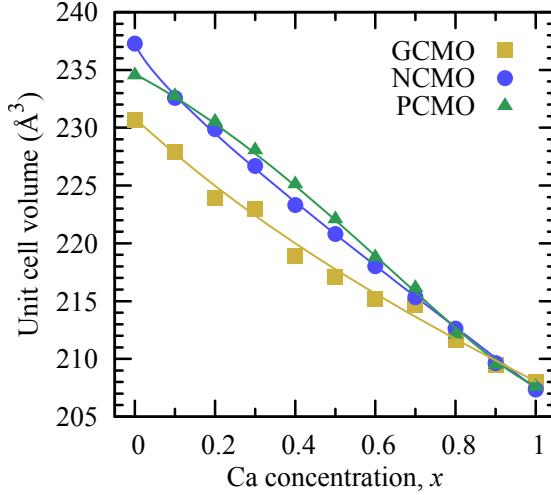


Figure 3. The room temperature unit cell volumes of  $\text{Gd}_{1-x}\text{Ca}_x\text{MnO}_3$  (GCMO),  $\text{Nd}_{1-x}\text{Ca}_x\text{MnO}_3$  (NCMO) and  $\text{Pr}_{1-x}\text{Ca}_x\text{MnO}_3$  (PCMO) as functions of the Ca concentration,  $x$ . The solid lines are a guide for the eye. Most of the linear trend seen in each dataset can be attributed to the decrease of cooperative JT distortion upon increasing  $x$ .

ties of manganites [5, 6]. With this in mind, one can certainly also appreciate the additional complication that manganites tend to develop oxygen vacancies e.g. under typical ceramic synthesis conditions [38–42]. In addition to breaking individual Mn–O–Mn bond chains, removing oxygen also significantly shifts the average Mn valence as indicated by the full compositional formula,  $L_{1-x}^{3+}M_x^{2+}\text{Mn}_{1-x+2\delta}^{3+}\text{Mn}_{x-2\delta}^{4+}\text{O}_{3-\delta}^{2-}$ , and thereby modifies the JT distortions.

The relative significance of the JT distortions is perhaps easiest to showcase by plotting the crystallographic unit cell volumes of entire manganite families over  $x$ , as in figure 3. In particular, based on the case of  $\text{Pr}_{1-x}\text{Ca}_x\text{MnO}_3$ , where the  $A$  site ions Pr and Ca are almost identical in size [29], one can deduce that the total effect of the JT distortions is to increase the cell volume by more than 10%, and the volume decreases linearly with increasing  $x$ . Simultaneously, the unit cell turns from distinctly orthorhombic (at  $x \leq 0.5$ ) to practically cubic (at  $x = 1.0$ ) [43].

## 2 Magnetism of manganites

### 2.1 Magnetic exchange interactions

In contrast to "everyday" macroscopic magnetic interactions that can typically be described in terms of Maxwell's equations and magnetic dipole moments, the magnetic structure of condensed matter is almost invariably governed by atom-level electron exchange interactions. These purely quantum mechanical interactions can be viewed as a complex consequence of Pauli repulsion between proximate electron quantum states [20].

In general, solving the exchange interactions in condensed matter is a formidable task and typically calls for sophisticated *ab initio* calculations, especially for complex oxides like manganites [5, 6] [P4]. However, useful heuristics have been developed for explaining the magnetostructure of manganites in terms of the results of small scale calculations involving only a handful of atoms at a time. Sufficiently restricted by design, these models can often be justified quite rigorously *ab initio* within their intended range of applicability [5, 6].

In line with the theme of this thesis, the most important types of exchange interactions encountered in manganites can be categorized by the length scales over which they operate: **(i)** the intra-atomic *Hund exchange* (HE), **(ii)** the inter-atomic *superexchange* (SE) and *double exchange* (DE) and **(iii)** the *exchange spring* (ES) mechanism that magnetically connects neighboring crystallites [5, 6, 44]. It should be noted that predictions of the magnetic structures of manganites are almost invariably attempted in terms of the Mn spins only, dismissing any magnetic moment at the *A* site as a small correction due to its weak coupling with the Mn network. While this can often be seen as a case where the ends indeed justify the means [5, 6], it is prudent to realize that most lanthanoid ions are in fact quite magnetic, and the following discussion may be fundamentally insufficient e.g. for describing manganites that contain Gd, Tb or Dy, the most magnetic lanthanoids [20, 45].

In the field of manganites, the general result regarding **(i)** is that the HE coupling can, by default, always be assumed to be strong enough to keep the Mn ions in the high spin state, i.e. with all unpaired *3d* electron spins parallel [6]. The ES, on the other hand, can be described as an extension of **(ii)** across lattice discontinuities [44]. With these points in mind, it will benefit one's



understanding to analyze the interatomic spin couplings in some detail.

Based on the discussion in subsection 1.2, we immediately observe a major difficulty in determining exchange interactions between the Mn sites: there are O atoms in between, so direct exchange [20] is not applicable. On the other hand, we are relieved by the experimental fact that spin-orbit interactions are negligible in manganites, so antisymmetric (or Dzyaloshinskii–Moriya) interactions need not be considered [6]. Between these extremes in complexity, the mutually complementary mechanisms of SE and DE have been proposed.

SE has been a very successful concept in explaining the magnetic structures of many materials where an indirect exchange interaction is present between two magnetic ions separated by a single nonmagnetic ion, such as  $O^{2-}$  [32, 46, 47]. In manganites, SE can be thought of as an ever-present "background" interaction, the overall character of which is antiferromagnetic (AFM) [3, 4, 48]. The origin of SE in manganites lies in the two  $2p$  valence electrons of  $O^{2-}$  which have a strong energetical incentive (due to Pauli repulsion [20]) to keep their spins antiparallel at all times. Each of these electrons will also form either a (partial) covalent bond or an ionic bond with one of the neighboring Mn ions, depending on the availability of an occupied Mn  $3d e_g$  orbital directed towards the particular  $O^{2-}$  ion [46, 47].

Two electrons that share a covalent bond orbital will have their spins strongly AFM-coupled to each other, whereas the direct exchange across an ionic bond (i.e. between orthogonal orbitals) will favor a weak FM coupling of the O and Mn electron spins. Due to the strong HE interaction, all  $3d$  electrons of a given Mn ion will always be parallel to each other. From these premises one can see that if both O–Mn bonds are of the same type, either covalent or ionic, then the total Mn–Mn SE is antiferromagnetic (weaker in the ionic case), and otherwise a (relatively weak) ferromagnetic (FM) coupling is formed. A schematic of this pattern of SE interactions, sometimes referred to as the Goodenough–Kanamori–Anderson rules, is shown in figure 4. In practice, when all possible SE interactions between the Mn sites are analyzed, the net character is almost always AFM [46, 47].

In contrast with SE and despite its name, the DE mechanism (as understood in modern literature [6]) does not only describe a magnetic exchange interaction, but also establishes a relation between ferromagnetism and metallic conductivity in manganites. In particular, the DE model explains why all

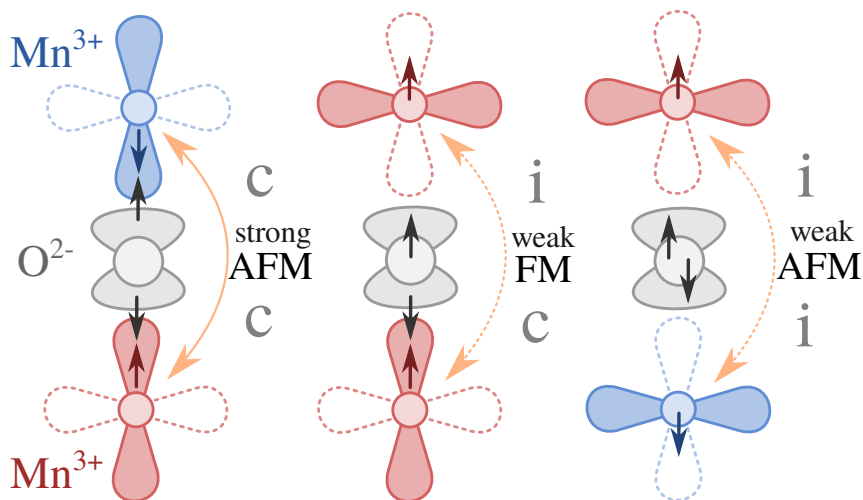


Figure 4. The three basic possibilities for SE interactions across a Mn–O–Mn bridge. Some Mn  $3d e_g$  orbitals of  $3z^2 - r^2$  symmetry and the participating O  $2p$  orbitals are shown for these examples. The Mn orbitals with dashed outlines are unoccupied. The single-headed arrows depict the expected positions and spin projections of valence electrons, with colors corresponding to the primary host atom of each electron. The Mn–O bond can be dominantly either covalent (c) or ionic (i). The exchange between Mn and O spins is weakly FM between orthogonal orbitals that form an ionic bond, and strongly AFM over a covalent bond. The total Mn–O–Mn interactions, written out in the figure for the depicted simple cases, can then be deduced from these rules.

metallic manganites in the hole doping region,  $x \leq 0.5$ , are ferromagnetic (although the converse is not true, as has been shown experimentally [5, 43]). The model is built on the following premises: the localized spin of Mn  $3d t_{2g}$  electrons can be treated classically, and there are "conduction" electrons, often identified with the Mn  $3d e_g$  electrons, that couple ferromagnetically to the  $t_{2g}$  spins and can hop from Mn site to Mn site [4, 22].

Thus, the DE mechanism is described by the Hamiltonian

$$H_{\text{DE}} = - \sum_{i,j} \tau_{ij} c_i^\dagger c_j - J_{\text{HE}} \sum_i c_i^\dagger \boldsymbol{\sigma} c_i \cdot \mathbf{S}_i. \quad (3)$$

Here the indices  $i, j$  refer to Mn sites in the crystal lattice. The hopping amplitude,  $\tau_{ij}$ , is typically assumed to be a global constant,  $\tau_{ij} = \tau$ , between nearest Mn neighbors, and  $\tau_{ij} = 0$  otherwise.  $c_i = (c_{i\uparrow}, c_{i\downarrow})^\top$  is the electron annihilation operator on the Mn site  $i$ , and  $c_i^\dagger$  the corresponding creation operator.  $\mathbf{S}_i$  is the classical  $t_{2g}$  spin at the site  $i$  and  $c_i^\dagger \boldsymbol{\sigma} c_i$  the conduction electron spin, where  $\boldsymbol{\sigma} = (\sigma^x, \sigma^y, \sigma^z)$  is the vector of Pauli matrices.  $J_{\text{HE}}$  represents the magnitude of the intrasite HE interaction. Note that the modern interpretation of DE does not explicitly address the details of the hopping conductivity mechanism, even though the "double" part in the name refers to one particular mechanism that was originally proposed [49] and later marginalized [6]. *Polaron hopping* models are typically invoked to explain the details of the observed conductivity of manganites [4–6].

In practical terms, the qualitative success of the DE mechanism in explaining the phase diagram and magnetoresistance of many manganite families [3–6] suggests that regardless of the details, an electron transport mechanism exists in manganites that allows the effective hopping of Mn  $3d e_g$  electrons from Mn<sup>3+</sup> ions to the empty  $e_g$  orbitals of neighboring Mn<sup>4+</sup> sites. In effect, one such hop swaps the valences of the participating Mn ions. Importantly, the effective hopping amplitude (or transition matrix element),  $\tau_{\text{eff}}$ , strongly depends on the angle,  $\theta$ , between the neighboring Mn  $3d t_{2g}$  spins,  $\mathbf{S}_i$ . The amplitude is maximized to  $\tau_{\text{eff}} = 4\tau/5$  at  $\theta = 0^\circ$ , and minimized to  $\tau_{\text{eff}} = \tau/5$  at  $\theta = 180^\circ$ . In a classical approximation, the relation can be written as  $\tau_{\text{eff}} = \tau \cos(\theta/2)$  [4]. The kinetic contribution to the free energy of the system is therefore minimized (i.e. made most negative) when the neighboring Mn spins align ferromagnetically.

At suitable values of  $J_{\text{HE}}$  and  $\tau$  the DE model successfully reproduces the metallic ferromagnetic phase that occupies a large portion of the magnetic phase diagram of manganites [5, 6]. However, recent theoretical and computational developments have also shown the DE mechanism to be capable of supporting much more exotic types of magnetic order, in particular, a host of highly frustrated, helimagnetic structures [22]. Their stability vs. the normal ferromagnetic structure, as well as the overall significance of DE over SE, strongly depends on  $\tau$ , which is essentially proportional to the Mn–O orbital overlap integrals. For this reason, basically due to the kinetic term in  $H_{\text{DE}}$ , the Mn–O–Mn bond geometry largely dictates the balance of magnetic exchange interactions in manganites, favoring DE when the bonds are as straight as possible, and SE otherwise [3–6].

## 2.2 The magnetic phases of manganites

Despite continuing advancements in *ab initio* techniques and models that are beginning to bridge the gap between the theoretical treatment and experimental observations of manganites [5, 21, 22, 24] [P4], many details of the general magnetic phase diagram of manganites are still understood solely on the basis of physical experiments and their immediate, often phenomenological interpretations. In all its diversity, the current situation could certainly benefit from a few swipes of Occam’s razor. With that in mind, however, there are nowadays sound theoretical, experimental and pedagogical reasons to present the magnetic phase diagram of manganites in two separate layers of abstraction: the *macroscopic* phase diagram, which reports "average" magnetostructures [P4] readily observable via standard bulk analysis methods, and the underlying *microscopic* phase diagram, which is more difficult (although entirely possible [50]) to observe directly and is characterized by dynamic variations of magnetic phase equilibrium across very small spatial length scales [6].

There is some room for debate [22] regarding whether it is of any use to consider the two layers separately throughout the phase diagram, or only in certain parts of it where several experiments and calculations confirm the presence of individual nanoscale magnetic clusters, of which the average magnetostructure is seen to be built [5, 6, 21, 50]. An attempt will be made to keep the following discussion neutral in this sense, although experimental observations of magnetic phase separation have sporadically been popping up all around

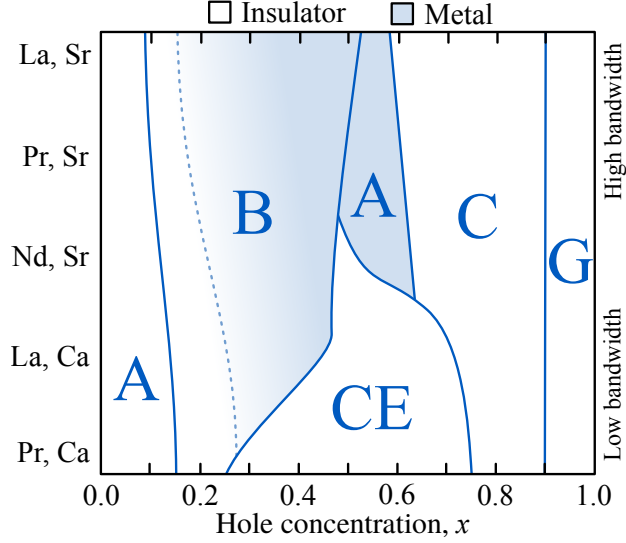


Figure 5. The macroscopic ground state magnetic phase diagram of manganites with respect to the Mn 3d conduction electron bandwidth (identified by the corresponding A site cations) and the hole concentration,  $x$ . The regions are labeled by the dominant type of magnetic order. Manganites in the shaded regions exhibit metallic conductivity, others are insulating or semiconductive. The FM region, B, contains species of both conductivity types, and the approximate border between the two is indicated by the dashed line. The regions other than B correspond to different AFM configurations shown in figure 6. Adapted from [53].

the phase space, somewhat in favor of the former approach [51, 52] [P4].

Figure 5 shows the macroscopic ground state magnetic phase diagram of manganites [53] with respect to the hole concentration,  $x$ , and the Mn 3d conduction electron bandwidth (BW). Examples of A site element pairs that yield particular points along the BW axis are also included: e.g. (Pr,Ca)MnO<sub>3</sub> has one of the lowest BW values among manganites, (La,Sr)MnO<sub>3</sub> one of the highest. The regions in the phase diagram are labeled by the average ground state magnetostructures of the Mn sublattice [P4]. The notation, based on the set of elementary structures presented in figure 6, follows what could be seen as the *de facto* standard in the field of manganites [6, 54]. Note that these structures are only a highly simplified presentation of the essential features of the magnetic space groups that are in practice used to model the magnetostructures (see section 3.2.2).

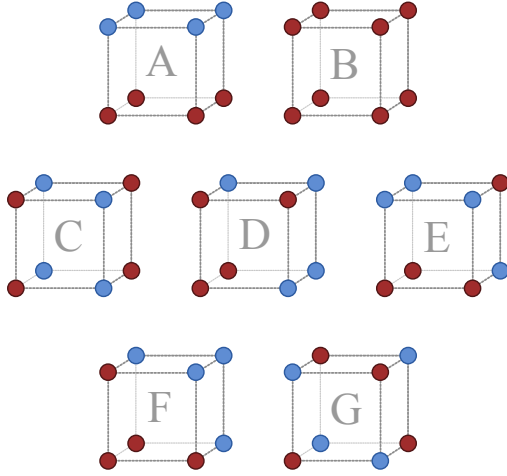


Figure 6. The elementary magnetic structures [54] often used to describe manganites. For clarity, only one octant of the general unit cell is shown in each case. The red and blue balls indicate the signature of Mn spin pseudovectors: spins of the same sign are collinear and spins in the red sublattice are antiparallel to those in the blue sublattice. The structure B is fully FM, the others correspond to specific AFM arrangements.

The magnetic phases A, B, C and G have relatively simple symmetries. B and G can be thought of as the end points of this series: B is FM and G is AFM in all three dimensions (3D). In between, the phase A is FM in 2D planes which are AFM-coupled along the third axis, and C is antiferromagnetic in 2D planes, but FM along the third axis. Due to the prevalence of the DE mechanism (see section 2.1) one should also constantly keep the electronic transport character of the phases in mind. Regarding this, one can observe (figure 5) that both A and B can support metallic transport in their ground state, but in the  $(\text{Pr}, \text{Ca})\text{MnO}_3$  system, or the low-BW end of the dataset, the ground state conductivity is of the activated type (i.e. the Fermi level is within an energy gap<sup>2</sup>) regardless of  $x$  [3, 5, 6, 43].

Both in terms of symmetry and physics, things arguably get the most interesting in the CE region of the phase diagram (figure 5). This ground state is often referred to by the backronym "charge exchange", but in line with the original treatment of Wollan and Koehler, one can in fact literally interpret it

<sup>2</sup>Note that this is only true near the ground state. For example, close to room temperature, the energy gap of PCMO  $x \approx 0.8$  reportedly vanishes completely [43].

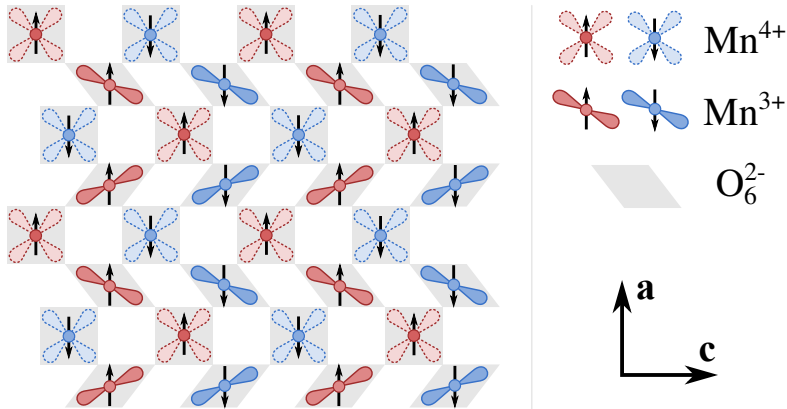


Figure 7. A schematic of the CE magnetostructure along the  $ac$  basal plane of the underlying  $Pnma$  crystal lattice (typical for half-doped manganites). Along the  $b$  axis, the CE structure repeats itself except for the spins which are flipped between layers. Charge, magnetic and orbital ordering can be seen. Occupied (unoccupied) Mn  $3d e_g$  orbitals are indicated by lobes with solid (dashed) outlines. Notice the elongation of the projections of the  $O_6^{2-}$  octahedra (grey quadrilaterals) around the JT active  $Mn^{3+}$  ions.

as a superposition of the C and E arrangements (figure 6), more completely written as  $C_{0.5}E_{0.5}$  in terms of abstract weight fractions [6, 43, 54]. Analogous expressions of the form  $C_xE_{1-x}$ , where  $x$  can again be identified as the hole concentration, have also been used to describe incommensurate departures from the ideal CE case [53, 55]. A schematic of the ideal CE structure is shown in figure 7.

In many ways, the most important traits and consequences of DE are culminated in the CE structure (and the nearby  $C_xE_{1-x}$  structures). Due to DE, simultaneously with the formation of the magnetic CE structure (which often occurs around  $T_N \approx 160$  K), an ordered pattern of the valences and  $3d$  valence electron orbitals of the Mn ions becomes energetically favourable. The geometries of all three ordering modes – magnetic, charge and orbital – are depicted in figure 7. In effect, a JT polaron [4, 5, 12] is formed around each  $Mn^{3+}$  ion, trapping the flow of charge and making the material insulating. This is a significant feature, because as one can see in figure 5, the metallic A and B phases directly border the CE region in the phase diagram, and the free energies of all three structures are, in fact, extremely close to each other [6].

To put things simply, it is precisely the mutual proximity of the metallic FM phase and the insulating CE-AFM phase which provides the mechanism for the CMR effect in low-BW manganites. However, simply the activation of DE-mediated conductivity if the Mn–O–Mn bonds were homogeneously straightened by an applied magnetic field is not enough to explain the magnitude of the CMR effect – there is a factor of at least about  $10^5$  missing from the observed changes in resistivity [4, 6, 7]. This brings us to the necessity of moving from macroscopic phase diagram down to the microscopic one.

The previously mentioned polaron formation around  $\text{Mn}^{3+}$  in the CE-AFM phase implies that there is a barrier of latent heat separating the CE-AFM and FM phases, i.e. the transition between these two is of the first order. Put in another way, both phases are at least metastable in the vicinity of the transition, and a spatial phase separation can take place. Should that happen, the CMR effect could elegantly be interpreted as the sudden percolation of the metallic FM phase through the insulating CE-AFM matrix, and remarkably, this is exactly what the experiments indicate [9, 56, 57]. The real surprise comes when trying to characterize the phase equilibrium dynamics in more detail, as it turns out that to do that, we need to stretch the concept of a thermodynamical phase somewhat [6, 58]. Namely, the FM and AFM "phases" have been determined to exist in clusters sized as little as a few nanometers across. In addition to sound theoretical arguments [5, 21] this view, no matter how upsetting it may seem at first, has been cemented by several experimental techniques, including neutron scattering [51, 52] [P4] and, quite recently, direct imaging by low-temperature Lorentz microscopy and electron holography [50].

There is nowadays little doubt that the FM–AFM phase separation model contains the essence of the physics of the CMR phenomenon [5, 6]. As mentioned above, it remains more debated (or has been so for the last decade) whether a similar scheme can consistently be extended over larger portions of the macroscopic phase diagram. The primary adversary to this approach is, of course, Occam's razor, but its benefits include the possibility to explain e.g. the insulating FM region at the low-BW end of the macroscopic phase diagram (figure 5) and some of the intricacies of magnetic hysteresis observed at extremal hole concentrations [51, 52] [P4]. The basic justification for the more general phase separation approach lies in the observation that regardless of any other order parameters, the orbital ordering related to cooperative JT



distortions (see section 1.2) is a dominant feature of many manganite families, especially towards the low-BW side of the macroscopic phase diagram, and a latent heat barrier is always associated with such lattice distortions [3–6]. It would naturally benefit the field of manganites greatly if the latest *ab initio* models could eventually catch up with these sometimes slightly speculative propositions.

### 2.3 The magnetocaloric effect

One of the journal articles included in this thesis [P3] explores magnetic entropy changes, an element of the *magnetocaloric effect* (MCE). Any material whose temperature observably changes when the material is subjected to a (slowly) changing magnetic field is said to exhibit the MCE [59–62]. Actually this covers almost all materials that can undergo a magnetic transition of any kind, but the magnitude, and thus usefulness, of the MCE greatly varies from material to material [62].

The physical basis of the MCE can be understood via the second law of thermodynamics: the total entropy of an isolated system cannot decrease in any process. When an external magnetic field,  $\mathbf{H}_{\text{ext}}$ , is applied on an unmagnetized piece of FM or ferrimagnetic (FiM) material, however, all of the material's elementary magnetic moments are aligned collinearly to the field (at least to a certain degree, determined by the magnitude of  $\mathbf{H}_{\text{ext}}$ ), effectively decreasing the number of degrees of freedom and thus the entropy of the spin lattice(s). It is then implied that at least a corresponding amount of entropy must have been generated elsewhere, and if the magnetic field was applied quickly enough to make the process adiabatic, the missing entropy can be found in the immediately adjacent ion lattice, whose temperature has just increased accordingly [59].

If the magnetocaloric material is kept thermally insulated from its surroundings while magnetized and the magnetic field is subsequently adiabatically removed, the entropy changes are reversed and the material returns to its original state. However, were a thermal contact with a heat sink made after the material is magnetized, and severed before the demagnetization, the material would actually exit the process at a lower temperature than at which it entered, providing the basis for a refrigeration cycle in analogy with ordinary gas expansion refrigerators [62]. For purely scientific applications, "one shot"

adiabatic demagnetization refrigerators which only utilize one half of the cycle have already seen decades of successful service [59].

Theoretical estimates place the maximum energy efficiency of magnetocaloric refrigerators at around 60% of the ideal Carnot efficiency, significantly higher than the 40% maximum of conventional gas refrigerators [59]. For this reason, driven by the increasing energy expenses related to refrigeration and air conditioning, a worldwide search for suitable magnetocaloric refrigerant materials is ongoing [61], and among others, magnetic oxides like manganites have received a great deal of attention [63]. Though the restricted availability of rare earth elements can be seen to weigh down on manganites somewhat, manganites often fare well in terms of other requirements posed for potential magnetic refrigerants, including a moderate heat capacity, low electrical conductivity, good chemical stability, etc. [59, 61–63]

Before anything else, though, the first prerequisite for a useful magnetic refrigerant is the presence of a magnetic transition within the intended operating temperature range. Furthermore, the transition must strike a balance between the contradictory requirements of being both sharp and wide over temperature, as quantified by the entropy change,  $\Delta S$ , and refrigerant capacity,  $\mathcal{RC}$ , respectively:

$$\Delta S(T) = \mu_0 \int_0^{H_{\max}} \left( \frac{\partial M}{\partial T} \right)_H dH \quad (4)$$

$$\mathcal{RC} = \int_{T_{\min}}^{T_{\max}} |\Delta S(T)| dT. \quad (5)$$

Here  $T$  is the temperature (K),  $\mu_0$  the permeability of vacuum ( $\text{TmA}^{-1}$ ),  $H$  the magnetizing field ( $\text{Am}^{-1}$ ) and  $M = M(H, T)$  the magnetization ( $\text{Am}^{-1}$ ).  $H_{\max}$  is the maximum magnetizing field to be used, and  $T_{\min}, T_{\max}$  can be taken to delimit the full width at half maximum (FWHM) of the peak in  $\Delta S(T)$  associated with the particular magnetic transition<sup>3</sup> [59, 63]. A similar expression can also be derived for the actual adiabatic temperature change,  $\Delta T_{\text{ad}}$ :

$$\Delta T_{\text{ad}} = \mu_0 \int_0^{H_{\max}} \left( \frac{T}{c_{p,H}} \right) \left( \frac{\partial M}{\partial T} \right)_H dH. \quad (6)$$

The  $\Delta T_{\text{ad}}$  values predicted by this formula are often quite realistic, provided

---

<sup>3</sup>This choice of  $T_{\min}, T_{\max}$  is typical when  $\mathcal{RC}$  is defined as a material property. However, an analogous quantity can be used for assessing the performance of an actual refrigerator device.  $T_{\min}, T_{\max}$  should then correspond to the operating temperature range of the device instead.

that the specific heat capacity at constant pressure and magnetic field,  $c_{p,H}$ , is known accurately. However, to quantify the magnetocaloric effect as reliably as possible, it is typically preferable and more practical to build a calorimeter around an adiabatic magnetization setup and measure  $\Delta T_{\text{ad}}$  directly [59, 64].

Both  $\Delta S$  and  $\mathcal{RC}$  are readily measurable by standard bulk magnetometers as a part of the standard characterization of magnetic materials, so it is useful to include them in the analysis in order to not miss any promising refrigerant candidates. The  $\Delta S(T)$  curves, and particularly their extrema, also convey a quick overview of the basic properties of the most important magnetic transitions in a given dataset. For example,  $\Delta S(T)$  typically peaks very close to the Curie temperature of ordinary ferromagnets, where the spin lattice is at its "softest" and easily responds to changes in  $H$ . In the vicinity of PM–AFM transitions, on the other hand, one can systematically find two  $\Delta S(T)$  peaks, one on either side of the transition. The one of these at the lower  $T$  will correspond to an intriguing *inverse* MCE where increasing the magnetic field actually decreases the temperature [62, 65] [P3].

## 3 Experimental details

### 3.1 Sample preparation

In the course of this work, polycrystalline PCMO samples were produced by two different synthesis routes, aiming at radically different crystallite sizes in the final product. Conventional solid state ceramic methods were applied for making powders and sintered blocks of PCMO where the maximum spatial dimension,  $D$ , of the crystallites was around  $1\ \mu\text{m}$ . A slightly more involved citrate gel autocombustion route was devised to arrive at nanocrystalline powders, with  $D \approx 40\ \text{nm}$ .

#### 3.1.1 Microcrystalline samples: Ceramic solid state synthesis

The traditional ceramic method, also referred to as solid state synthesis [66], lends itself very well for the synthesis of PCMO, as PCMO turns out to be by far the most stable compound in its region of the (Pr,Ca,Mn,O) phase diagram under the suitable sintering conditions. The following synthesis scheme was designed to avoid just one major pitfall: the formation of the spinel structured manganese oxide  $\text{Mn}_3\text{O}_4$ , a typical magnetic impurity phase in manganites [67–71] [P4]. The key point for achieving this lies in performing a careful initial calcination of the metal oxide mixture. One should note that the following approach has only been optimized for chemical phase purity, completely disregarding e.g. grain morphology.

Oxides and carbonates are preferable starting materials for ceramic synthesis, because they are typically quite safe to handle and can be weighed reliably once certain precautions are taken. For PCMO, analytical grade  $\text{Pr}_{12}\text{O}_{22}$ ,  $\text{CaCO}_3$  and  $\text{Mn}_2\text{O}_3$  or  $\text{MnO}_2$  were used. All of these tolerate drying at  $200\ ^\circ\text{C}$  (or actually even at  $500\ ^\circ\text{C}$ , above which  $\text{CaCO}_3$  burns into  $\text{CaO}$ ) without changing their composition, so it is recommended that they be dried overnight at this temperature. In general, lanthanoid oxides are highly hygroscopic and can develop a significant hydroxide contamination within hours of contact with ambient air. They should therefore be properly calcined (at ca.  $1300\ ^\circ\text{C}$ ) immediately prior to weighing, but  $\text{Pr}_{12}\text{O}_{22}$  appears to be exceptionally stable against such contamination, so typically a simple drying treatment will suffice for it. Nevertheless, the starting reagents should always be carefully characterized by a routine x-ray diffractometry (XRD) analysis (see section 3.2.1) prior

to starting a new synthesis project.

PCMO can very well be calcined and sintered in air (except for the  $x = 1.0$  endpoint which calls for pure  $O_2$  [P1]), where its oxygen content will equilibrate with that of the surrounding atmosphere. Stoichiometric calculations therefore only need to take into account the amounts of Pr, Ca and Mn. Once the stoichiometric amounts of oxides and carbonates have been weighed, they should be carefully mixed by mortaring (or an equivalent technique) and compacted into pellets to maximize the contact between grain surfaces. This will help facilitate the intergrain diffusion of ions, which is the main principle behind the ceramic synthesis method [66].

The temperature of the initial calcination should be chosen so that  $CaCO_3$  readily decomposes into  $CaO$ , but the Mn oxide is not spontaneously reduced to  $Mn_3O_4$ . 60 h at  $750^\circ C$  has been found good for the calcination. The heating rate should be gentle, no more than about  $100^\circ C/h$ , to minimize the mechanical stresses on the sample. At the end of the calcination program one can simply cut the power to allow a reasonably rapid passive cooldown to take place. The calcined pellets should be crushed and mortared again to improve mixing, recompact, and then subjected to sintering. Using an alumina substrate, sintering at  $1300^\circ C$  for 24 h is to be recommended. Ramp rates similar to the calcination sequence can be used. Calcined PCMO typically needs to be crushed, mixed and sintered three times before its structure no longer significantly changes in the process (as verified by XRD), indicating the synthesis is complete.

### 3.1.2 Nanocrystalline samples: Citrate gel autocombustion

The following method can be seen as a variant of sol-gel synthesis, where the general idea is to condense a stoichiometric solution of metal cations into a gel, which is then calcined to yield a desired oxide material [72]. The strong points of this approach are the atomic-level mixing of the constituents during the solution phase, and that unless a special substrate is used, decomposing the gel usually yields very small, nanoscale particles, or even a partially amorphous powder, as in our case. The following recipe is particularly specialized for the purposes of a laboratory where ceramic synthesis is the norm, as instead of metal nitrates (the usual, preferable starting materials [73]), this approach starts with a (somewhat crude) process of converting stock metal oxides and

carbonates into soluble form.

To begin, stoichiometric amounts of Pr, Ca and Mn oxides or carbonates need to be weighed as in section 3.1.1. An amount of citric acid monohydrate,  $C_3H_5O(COOH)_3 \cdot H_2O$ , equivalent to the combined amount of metal cations, i.e.  $n(Pr) + n(Ca) + n(Mn)$ , is also weighed. The materials are placed into a heat-resistant beaker and covered with 65% nitric acid,  $HNO_{3(aq)}$ . This, and all of the following steps, must be performed within a fume hood due to the release of toxic nitrogen oxide gases.

A continuous magnetic stirring is initiated on a hot plate set to  $300^\circ C$ . Within 15 min the mixture should begin to clear up into an orange solution. Once the mixture has completely turned from translucent to transparent, an additional mixing time of at least another 15 min should be allowed to ensure the homogeneity of the newly formed solution. Then the heat can be turned off. Next, the pH value of the solution is adjusted to 5 using ammonia,  $NH_{3(aq)}$ . The process can be monitored with universal indicator paper, and will be accompanied by a change of solution color from orange to green to pale yellow. In case the pH overshoots the target value, a visible precipitation will occur, which one may attempt to counter by administering additional  $HNO_{3(aq)}$ . Once the solution is at  $pH \approx 5$ , an amount of ethylene glycol,  $C_2H_4(OH)_2$ , equal to  $4n(C_3H_5O(COOH)_3 \cdot H_2O)$  is to be added to assist in the formation of the gel. The gelation can be achieved by leaving the solution on a hot plate at  $200^\circ C$  for three days without mixing.

The dry gel must be handled with utmost care, and always within a fume hood, because it is a subsonic explosive. An oxidizer-rich mixture of nitrates and organic compounds, the gel will readily autoignite between  $220^\circ C$  and  $500^\circ C$ , and deflagrate with a sudden release of nitrogen oxides and amorphous PCMO powder. To calcine the gel in a controlled manner, one should use a well ventilated furnace heated to  $500^\circ C$ , and process the gel in batches no larger than  $10\text{--}15\text{ cm}^3$ . For best results, the gel should be carefully mortared prior to calcination, and allowed to react for at least 5 min in the furnace. The gel will ignite within 1–2 min when exposed to this temperature. To crystallize the amorphous PCMO precursors thus obtained, they should be annealed at  $700^\circ C$  for 6 h. This will yield a mixture of nanocrystalline PCMO and  $Pr_{12}O_{22}$ , roughly at a ratio of 4:1 by mass. The purity can be improved with respect to PCMO by further annealing, indicating that some amorphous Ca and Mn

oxides will initially remain in the mixture in addition to the two most readily crystallizing phases, but this will unavoidably also increase the PCMO crystallite size from the initial value of  $D \approx 40$  nm.

## 3.2 Sample characterization

A myriad of specialized techniques exist for the physical characterization of condensed matter. However, for magnetic oxide materials like PCMO, in particular, two basic characterization methods have proven to be indispensable: powder diffraction and bulk magnetometry [20, 74]. The former is well suited for determining the chemical purity and atomic scale structural properties of crystalline matter, whereas the latter can be used to outline the magnetic phase diagram of a material by measuring its magnetization vs. temperature and external magnetic field.

### 3.2.1 Powder diffractometry

*Diffraction* is the phenomenon where a propagating wavefront meets an obstacle and is locally bent into the region of geometrical shadow cast by the obstacle. If the size of the obstacle is comparable to the wavelength, the bent wavefront will essentially *interfere* with itself behind the obstacle as different parts of the original front become superposed. Moreover, if several obstacles are lined up in a periodic pattern, like the atoms in a crystal lattice, a predictable interference pattern that is unique to the spatial arrangement of the obstacles will be observed. This is the principle by which diffraction can be used to characterize crystalline materials. In real materials, the distances between atoms (an useful proxy for the "size" of atoms) are of the order  $1 \text{ \AA}$ , which matches well with the (de Broglie) wavelengths that e.g. electrons, neutrons and x-ray photons can exhibit at practically accessible energies.

Given an ideal crystal structure that repeats itself into infinity, one can construct various mathematical planes that each contain a certain infinite subset of the atoms in the structure. Due to the translation symmetry of crystals, identical copies of any such plane can then be found periodically, separated by some distance,  $d$ , along their normal. It can then be shown that as a consequence of diffraction, a set of atomic planes with normal separation  $d$  is able to produce a bright specular reflection when illuminated by coherent radiation

coming from a normal angle,  $\theta$ , that fulfills the following equation, known as the Bragg condition:

$$2d \sin \theta = n\lambda. \quad (7)$$

Here  $\lambda$  is the wavelength of the incoming radiation and  $n$  any positive integer. So every crystallite has its own set of possible specular reflections due to diffraction, and given a powder sample with enough randomly oriented crystallites, one can assume that all possible diffractive reflections are realized when the sample is illuminated. Thus, by measuring the reflected radiation intensity vs. the reflection angle,  $I(\theta)$ , over a circular arc which contains the radiation source and is centered around the sample, one can construct the distribution of atomic plane distances,  $d$ , in the crystal structure of the sample via equation (7) [74].

In the case of x-rays, the graph of  $I(d)$ , called a *diffractogram* in  $d$  space, can in fact be directly identified with the magnitude of the three-dimensional Fourier transform of the electron density of the crystal. It is then clear that the full lattice geometry cannot be reconstructed based on the diffractogram alone, but the inverse problem of predicting the diffractogram of a given lattice is solvable [74]. Thus it is possible to identify crystalline materials by comparing their diffractograms against ones generated from a database of known structures. In combination with a rough initial guess of the structure and advanced data analysis methods, like the Rietveld refinement method introduced in section 3.2.2, one can also attempt to solve the structure of an unknown material.

When solving crystal structures for the first time, the quality of the data becomes paramount. For modeling materials with elements heavier than Ne, XRD is indeed a very capable technique both in terms of  $d$  and  $I$  resolution, especially if synchrotron light sources are available. Even so, pairing XRD up with a complementary technique can be even more powerful. Neutrons, for example, do not significantly interact with the electron cloud, but with atomic nuclei and magnetic moments. The resolution of neutron diffractometers usually falls short of x-ray equipment with a similar build budget, but neutrons can e.g. easily resolve hydrogen and oxygen atoms, differentiate hydrogen from deuterium with exceptional contrast, and provide critical information regarding the magnetic structure of materials. Modern-day data analysis software typically facilitates the concurrent treatment of several diffractograms from multiple sources, allowing one to make the best out of complementary



datasets.

Laboratory XRD stations have the practical benefit over many spectroscopic characterization methods that the measurements can perfectly well be carried out in almost any atmosphere, including ambient air. On the other hand, advanced non-ambient sample chambers, like the ones used in this thesis work [P1] [P2], typically allow one to control at least the temperature of the sample, and possibly additional parameters such as the external magnetic field. Thus, phenomena such as thermal expansion, magnetostriction and structural phase transitions can be directly addressed via diffractometry. Both of the diffractometers used in this thesis work – the *Philips X'Pert Pro* laboratory XRD station at the Dept. of Physics and astronomy, University of Turku, and the *DMC*, a cold neutron diffractometer located at SINQ, Paul Scherrer Institute, Switzerland – were highly modular Bragg–Brentano type diffractometers [74] with multiple options for e.g. limiting the beam geometry and filtering the incident radiation wavelengths. For the best results given a limited beamtime, these aspects must be carefully tailored to maximize the reliability, interpretability and statistical significance of the results. The instrument configurations typically used in the present work are listed in table 1.

### 3.2.2 Rietveld refinement

It is quite straightforward to identify a pure crystalline material just by noting the pattern of  $d$  values at which diffracted intensity maxima are observed. With a knowledge of how  $d$  can be expressed in terms of the lattice parameters (this depends on the crystal symmetry [74]), one may even be able to determine the outer dimensions of the unit cell that repeats itself in the crystal structure [75]. However, due to the finite resolution of diffractometers, two or more reflections on a complicated diffractogram may partially overlap, and especially if multiple structural phases are present, it is often impossible to reliably determine the  $d$  coordinates of individual reflections, let alone the total symmetry of the structure, by eye. This is where *Rietveld refinement* typically comes into play [74, 76–78].

Rietveld refinement is a computational analysis technique where an initial guess for the complete crystal structure is used to generate a simulated diffractogram, which is then slowly evolved to better match the measured data. The refinement is typically implemented as a least squares fit with respect to the

Table 1. Typical configurations of the two diffractometers used in this work: the commercial Philips x-ray diffractometer and the DMC cold neutron diffractometer. Due to the highly modular structure of the instruments, most of these parameters can be tailored to the specific needs of each experiment. Note the vast difference in the ranges of accessible  $d$  values between the instruments. For a comparison of the time scales, the DMC's neutron monitor was observed to receive ca. 5500 counts per minute when the spallation source was fully operational.

	<b>Philips X'Pert Pro</b> University of Turku	<b>DMC</b> SINQ, PSI
Radiation	Cu $K\alpha$ x-rays 40 kV vacuum anode Ni foil filter $\lambda = 1.5418 \text{ \AA}$	cold neutrons continuous spallation source PG monochromator $\lambda = 2.45 \text{ \AA}$ or $4.20 \text{ \AA}$
Optics	Bragg–Brentano geometry 40 mrad Soller slits 4.4 mrad incident slit 10 mm incident mask 7.5 mm receiving slit	Bragg–Brentano geometry 20 mrad oscillating collimator 13 mm $\times$ 36 mm incident slit
Detection	1D silicon strip 14 mm arc, 255 channels timer scheduled	1D $\text{BF}_3$ counter bank 210 mm arc, 400 channels neutron monitor scheduled
Scan parameters	$0.9 \text{ \AA} \leq d \leq 4.4 \text{ \AA}$ $20^\circ \leq 2\theta \leq 110^\circ$ $\Delta(2\theta) = 0.026^\circ$ 15 min total time	$1.7 \text{ \AA} \leq d \leq 12.8 \text{ \AA}$ at $\lambda = 2.45 \text{ \AA}$ $2.9 \text{ \AA} \leq d \leq 21.9 \text{ \AA}$ at $\lambda = 4.20 \text{ \AA}$ $11^\circ \leq 2\theta \leq 93^\circ$ $\Delta(2\theta) = 0.10^\circ$ 148 600 total monitor counts
Sample environment	air or technical vacuum resistive heater $\text{LN}_2$ cold finger $83 \text{ K} \leq T \leq 683 \text{ K}$	He flushed vacuum resistive heater LHe cryostat $5 \text{ K} \leq T \leq 300 \text{ K}$ 2.8 T superconducting magnet

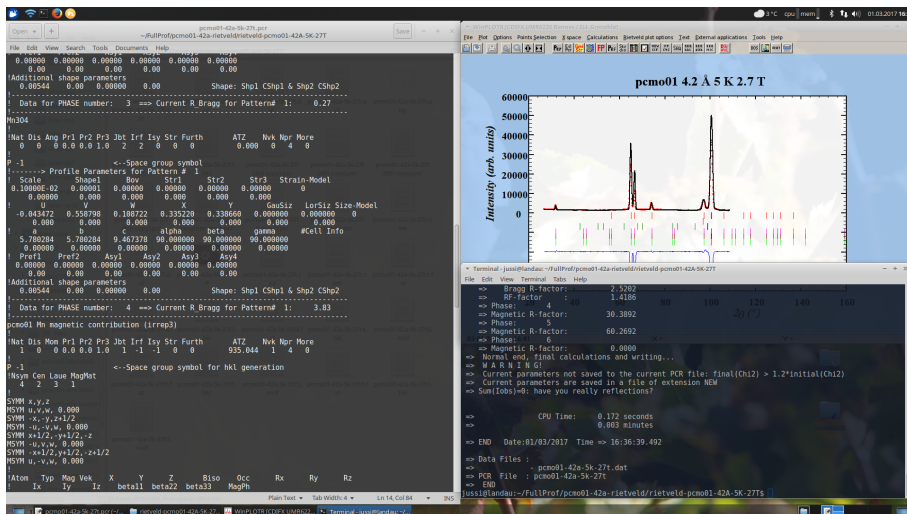


Figure 8. FullProf Rietveld refinement of  $\lambda = 4.2 \text{ \AA}$  cold neutron diffraction data in progress. The diffractogram (top right; visualized along with the fit, error curve and Bragg reflections) corresponds to a PCMO  $x = 0.1$  sample cooled down to 5K and placed under an applied magnetic field of 2.7T. The refinement program is controlled by a specially formatted input file (left) and run on the command line (bottom right). One unphysical magnetic phase proposed by the scientist has just been eliminated by the program, so several checks must now be made on the rest of the parameters to sort out any artifacts caused by proposing the false phase.

parameters of the diffractogram simulator, although other error functionals can also be used – in particular, the so-called maximum likelihood functional is more reliable if unidentified crystalline phases are present [77]. In fact, the quality of a Rietveld fit can (and often should) be assessed in terms of several parameters at the same time. Perhaps the most common overall indicator of the agreement between the observed and calculated data is  $\chi^2$ , the ratio between the error functional and an expected error sum derived from a model of the data acquisition process (often a Poisson process) [77, 78]. Once a refinement converges below  $\chi^2 = 2$ , the observations can be said to be explained by the fit in the statistical sense – unless  $\chi^2 < 1$ , which would imply the expected error has been overestimated [78].

The calculations required for Rietveld refinement are too time-consuming to be feasible by hand, so dedicated computer program packages have been developed for the task. Some of the better-known packages include FullProf [79], GSAS [80] and MAUD [81]. These can all be downloaded and used free

of charge and are light enough to run quite well on almost any desktop CPU. Figure 8 shows the FullProf package in action, in an early stage of the Rietveld refinement of a neutron diffractogram.

A Rietveld refinement typically begins with the declaration of a space group and a set of basis atoms. These determine the set of allowed Bragg reflections (as identified by their *Miller indices* [74]). The algorithm then proceeds to modify the positions,  $d_i$ , integrated intensities,  $I_i$  and shapes,  $I(d - d_i)$ , of individual reflections via an array of underlying variables. The parameters  $d_i$  are determined by the lattice parameters of the unit cell and a set of correction terms used to model the small geometrical faults of the diffractometer. The  $I_i$  are functions of the atomic positions within the unit cell, atomic occupancies, Debye-Waller factors [74] and possibly additional terms, such as corrections for preferred crystallite orientation. The peak shape is allowed to depend on  $d$  and can be based on a number of mathematical functions, the most common one of which is the pseudo-Voigt profile. This profile is a computationally efficient approximation to the convolution of Gaussian and Lorentzian functions, being a linear combination of the two instead. Information regarding the crystallite size and residual strain can be extracted from the refined profile shapes using various models [82].

As stated above, the strength of the Rietveld method lies in its ability to handle overlapping Bragg reflections. Taking this to an extreme, one can also use it to separately model the nuclear and magnetic contributions to a neutron diffractogram. The magnetostructural symmetries of crystalline materials can be described using a set of magnetic space groups known as the Shubnikov groups, which are derived from the underlying structural space groups with the addition of a time reversal operator [79]. Finding the correct Shubnikov group can take some effort, since especially for complex magnetic materials like PCMO, a single magnetic phase may not even be enough to explain the observed neutron diffractogram.

We are now finally in a position to define what it means for PCMO  $x = 0.5$  to have a magnetic structure of type  $C_{0.5}E_{0.5}$  [43]: to explain its neutron diffractogram, we simply must include an equal-weight superposition of C-AFM and E-AFM structures (see section 2.2) in the Rietveld model. Note that because the diffractogram is a sum of reflections collected from the entire sample, it does not tell us whether these two phases actually exist in spatially distinct re-

gions, or if the average spin structure is the real one and uniform throughout the sample. For PCMO  $x = 0.5$  in its CE-AFM state, the latter interpretation turns out to be correct, but the original neutron diffraction results had to be complemented by resonant x-ray scattering studies in order to firmly arrive at this conclusion [83].

### 3.2.3 Bulk magnetometry

Magnetometry can broadly be understood to encompass all empirical techniques capable of measuring some aspect of the magnetic field, be it the entire magnetic flux density vector  $\mathbf{B}$ , a subset of its components or possibly the total magnetic flux,  $\Phi$ , through a given surface. In the field of material physics, magnetometry often has the special role of being used to determine the magnetizations,  $\mathbf{M}$ , of materials.

Different methods of magnetometry have been developed for a variety of situations. Nuclear magnetic resonance can be used to determine the absolute magnitude of  $\mathbf{B}$  with remarkable precision, provided that the field is highly stable and homogeneous across the probe. If one is prepared to trade precision for ease of use and portability, a Hall effect sensor is a handy alternative. Somewhere between these two extremes in complexity one may find fluxgate magnetometers which typically cannot measure fields higher than a few mT, but are e.g. extremely well suited for examining geomagnetic fields due to their sensitivity and directionality. Techniques typically encountered in material physics labs also include the direct imaging of magnetic domains via magneto-optical Kerr effect microscopy, and inductive pickup coil magnetometers often embedded in cryostats with high-performance superconducting magnets [20].

This thesis work has heavily relied on two inductive pickup coil magnetometers, the *Quantum Design PPMS ACMS* in DC mode and the *MPMS XL RSO*. The principle of operation is the same in both: a few milligrams of sample material are suspended on a long, essentially nonmagnetic stick, which is lowered inside a set of inductive pickup coils, and moved there in a controlled way (roughly sinusoidal oscillation) to induce a voltage proportional to the sample's magnetic moment,  $\mu$ , into the pickup coils as governed by Lenz's law [20]. The graph of this voltage vs. the sample position is analyzed to extract the  $z$  component of  $\mu$ , based on calibration measurements of known magnetic

moments. The DC magnetometers of the ACMS and MPMS basically only differ by the way the signal from the pickup coils is amplified: the ACMS uses a conventional lock-in amplifier design with a moderate  $\mu$  resolution, whereas the MPMS employs a highly sensitive radio frequency superconducting quantum interference device (RF SQUID) inductively coupled to the pickup coils [20].

The pickup coils surround a temperature-regulated sample chamber that can be resistively heated slightly above room temperature (to 400 K) or cooled down to ca. 2 K using liquid He. The same cryogen keeps heavy-duty superconductor magnets that coaxially surround the sample chamber in operation, so that the magnetic moment can be measured vs.  $T$  and the applied magnetic field automatically. The technical parameters of the instrument configurations used in this work are summarized in table 2, and an example of a magnetic measurement sequence can be found in table 3. The technical reasoning behind the latter can be seen to mainly revolve around optimizing the data density vs. the consumption of time and cryogen resources, in addition to which specific steps are taken to ensure that both the sample and the instrument magnet are initially in a well defined state of (zero) magnetization, or *degaussed*. Proper sample degaussing is critically important if measurements are to be conducted close to or below the coercivity of the sample material, which can be up to 50 mT for most species of PCMO [17] [P1].

When measuring bulk powder samples, the most notable concern left for the experimentalist to bear is how to control the demagnetizing field,  $H_d$ , of the sample.  $H_d$  can be seen as the geometry-dependent component of the magnetic field generated by the sample, and must be addressed to be able to correctly determine the magnetization,  $M$ , of the sample. The  $z$  component of the total magnetic flux density through the sample can be written as

$$\frac{B}{\mu_0} = H + M = H_{\text{ext}} + H_d + M. \quad (8)$$

Here, in addition to the symbols defined above,  $\mu_0$  is the permeability of vacuum,  $H$  the magnetizing field and  $H_{\text{ext}}$  the external magnetic field. We wish to determine  $M$ , which should be a material property independent of the geometry. However, what we actually measure on a pickup coil magnetometer is the whole magnetic moment generated by the sample, that is,  $(M + H_d)V$ , where

Table 2. The basic technical parameters of the commercial Quantum Design magnetometers used in this work. Both were located at the Wihuri Physical Laboratory.

	<b>QD PPMS</b> ACMS DC magnetometer	<b>QD MPMS XL</b> RSO SQUID magnetometer
Signal pickup	induction to lock-in amp	induction to SQUID
Sensitivity range	$3 \cdot 10^{-8} \text{ Am}^2$ to $5 \cdot 10^{-3} \text{ Am}^2$	$1 \cdot 10^{-11} \text{ Am}^2$ to $1.5 \cdot 10^{-3} \text{ Am}^2$
Superconducting magnet	$-9 \text{ T} \leq \mu_0 H_{\text{ext}} \leq 9 \text{ T}$ accuracy 0.2 mT uniformity 0.01% / 5.5 cm	$-5 \text{ T} \leq \mu_0 H_{\text{ext}} \leq 5 \text{ T}$ accuracy 0.1 mT uniformity 0.01% / 4.0 cm
Cryostat	LHe in LN <sub>2</sub> sleeve resistive heater $1.9 \text{ K} \leq T \leq 350 \text{ K}$ $T$ stability 0.02% bore $\varnothing$ 25 mm	LHe in vacuum sleeve resistive heater $1.9 \text{ K} \leq T \leq 400 \text{ K}$ $T$ stability 0.5% bore $\varnothing$ 9 mm

$V$  is the volume of the sample. We can roughly approximate the demagnetizing field by  $H_d \approx -NM$ , where  $N$  is the geometry-dependent *demagnetization factor* in the range  $0 \leq N \leq 1$ . For ellipsoidal samples this approximation is in fact very good, and in particular, perfectly spherical samples will have  $N = 1/3$ . With a bit of algebra one can then see that  $H_d$  is by no means a small correction – omitting it will lead to  $M$  being directly underestimated by the factor  $N$ , which is typically several tens of percent. Unfortunately, determining  $N$  is somewhat difficult and in many cases the largest contribution to the absolute error of  $M$ . However, if the material under study happens to be a soft ferromagnet with a small coercivity compared to its saturation magnetization, one may attempt to find the upper limit of  $N$  by plotting  $M$  vs.  $H_{\text{ext}} + H_d$  at various values of  $N$ . If the demagnetization curve becomes multiply-valued, i.e. unphysical, the chosen  $N$  is too high [20].

Table 3. An example of a magnetic measurement sequence. These particular steps were taken with the nanoparticle samples described in [P5]. Here  $T$  and  $\mu_0 H_{\text{ext}}$  refer to the magnetometer's temperature and field settings, respectively, and  $m$  is the measured raw magnetic moment. FC and ZFC are standard acronyms for *field-cooled* and *zero-field-cooled*, respectively.

<b><math>M(T)</math> subsequence</b> using QD MPMS XL	<ol style="list-style-type: none"> <li>1. Start with the sample thermally demagnetized.</li> <li>2. Measure a ZFC–FC scan at <math>\mu_0 H_{\text{ext}} = 10</math> mT: <ol style="list-style-type: none"> <li>2a. Set <math>T</math> to 10 K.</li> <li>2b. Set <math>\mu_0 H_{\text{ext}}</math> to 10 mT.</li> <li>2c. Sweep <math>T</math>: 10 K <math>\rightarrow</math> 400 K <math>\rightarrow</math> 10 K, at 2 K/min.</li> <li>2d. While sweeping, measure <math>m</math> every 1 K.</li> </ol> </li> <li>3. Measure a FC scan at <math>\mu_0 H_{\text{ext}} = 1</math> T: <ol style="list-style-type: none"> <li>3a. Set <math>T</math> to 400 K.</li> <li>3b. Set <math>\mu_0 H_{\text{ext}}</math> to 1 T.</li> <li>3c. Sweep <math>T</math>: 400 K <math>\rightarrow</math> 10 K, at 2 K/min.</li> <li>3d. While sweeping, measure <math>m</math> every 1 K.</li> </ol> </li> <li>4. Repeat the FC scan at <math>\mu_0 H_{\text{ext}} = 2</math> T, 3 T, 4 T, 5 T.</li> <li>5. Set <math>T</math> control on standby and degauss magnet.</li> </ol>
<b><math>M(H)</math> subsequence</b> using QD PPMS	<ol style="list-style-type: none"> <li>1. Measure a <i>hysteresis loop</i> at <math>T = 10</math> K: <ol style="list-style-type: none"> <li>1a. Set <math>T</math> to 10 K.</li> <li>1b. Set <math>\mu_0 H_{\text{ext}}</math> to 8 T.</li> <li>1c. Sweep <math>\mu_0 H_{\text{ext}}</math>: 8 T <math>\rightarrow</math> <math>-8</math> T <math>\rightarrow</math> 8 T, at 19 mT/s.</li> <li>1d. While sweeping, pause 240 times at evenly spaced values of <math>\sqrt{ H_{\text{ext}} }</math>. This will yield a higher data density closer to the origin.</li> <li>1e. Measure <math>m</math> during each pause.</li> </ol> </li> <li>2. Measure additional hysteresis loops at <math>T = 30</math> K, 50 K, 70 K and 100 K.</li> <li>3. Set <math>T</math> control on standby and degauss magnet.</li> </ol>



## 4 Simulations

This thesis is mainly in the field of experimental physics, but at a few key points, the work has been significantly supported by computer simulations. For example, the physical validity of the neutron diffraction Rietveld refinement in [P4] was verified by comparison with computational *ab initio* models contributed by prof. Hergert's group. Their approach was to first perform detailed electronic band structure calculations using the Korringa-Kohn-Rostocker method [24], an application of *density functional theory* [84, 85], based on which a *Monte Carlo* (MC) simulation was run to solve the magnetostructure. The specifics of their state-of-the-art techniques are outside of the scope of the present thesis, but to acknowledge the general usefulness of MC simulations in physics [86, 87], the following sections 4.1 and 4.2 will introduce the basics of one particular MC method and its application in the micromagnetic simulation reported in [P5].

### 4.1 The Metropolis–Hastings Monte Carlo algorithm

In the mathematical sciences, MC methods refer to various ways of approximating a solution to a computationally intensive problem by making use of random sampling. Many optimization and integration problems can be formulated in ways suitable for MC approaches. At the simplest level, drawing a set of random samples from a known probability distribution can be seen as constructing a MC approximation to that distribution [87].

Physical problems, in particular, often lend themselves well to solution using so-called *Markov chain* MC techniques, where the system under study is evolved in random steps from an (arbitrary) initial state towards a solution that is known (or at least reasonably presumed) to be stable with respect to the evolution, such as the state of minimum free energy [87]. The Metropolis–Hastings (MH) algorithm is a particular classic among such techniques [86–89]. Although seldom the most efficient solution for any given problem, the pure simplicity of the MH algorithm should afford it a place in any simulation developer's toolkit, in addition to which it can readily be extended to implement more advanced solution schemes like *simulated annealing* [88].

The principle of the MH algorithm is to construct a Markov chain of states by assessing a series of *proposals*,  $X$ , regarding new states to be entered. There

are two layers of randomness involved in the process: how new proposals are generated (see section 4.2 for an example), and whether or not they are accepted. Preferably, the probability of acceptance,  $\mathcal{P}(X)$ , should depend on the content of the proposal  $X$  [86]. As a typical example, if the task is to minimize the energy of a simulated system, any proposal that is found to decrease the energy should always be accepted. However, to prevent the algorithm from getting stuck at shallow local energy minima, it is also beneficial to allow small increases in energy to occur from time to time. One very sensible way to attain this is to define  $\mathcal{P}(X)$  as the ratio of the Boltzmann factors of the proposed state (energy  $E_2$ ) and the current state (energy  $E_1$ ), i.e.

$$\mathcal{P}(E_1 \rightarrow E_2) = \exp\left(\frac{E_1 - E_2}{kT_{\text{sim}}}\right) \quad (9)$$

where the temperature term,  $kT_{\text{sim}}$ , does not necessarily need a physical interpretation, but is a technical simulation parameter to be adjusted by the programmer in order to reach a balance between the convergence rate of the algorithm and its ability to avoid local energy minima. One can see that using equation (9) may actually lead to proposals where  $\mathcal{P}(E_1 \rightarrow E_2) > 1$ , which, in accordance with the remarks above, should always be accepted<sup>4</sup>.

## 4.2 The mesoscale model of magnetic phase separation

Until the power of supercomputer grids reaches a level where enough atoms can be modeled from first principles to describe phase separation phenomena, the mechanism of the CMR effect of low BW manganites remains out of the direct reach of *ab initio* computational techniques [5, 6, 21, 24]. That being the case, *phenomenological models* that "average over" some of the physical details to arrive at an approximate semiempirical description may prove themselves valuable for establishing an operational understanding of the CMR effect.

This thesis work led to the development of a dynamic simulation of the mesoscale magnetic interactions and phases in low BW manganites, or more technically, a Metropolis–Hastings Monte Carlo simulation capable of reproducing the experimentally observed  $M(H)$  loops of PCMO, including the meta-

---

<sup>4</sup>Despite this apparent complication, equation (9) actually allows for an elegant implementation in programming code: to decide on a proposal, generate a uniformly distributed random floating point number  $x \in [0, 1)$  and accept if and only if  $x < \exp[(E_1 - E_2)/(kT_{\text{sim}})]$ .

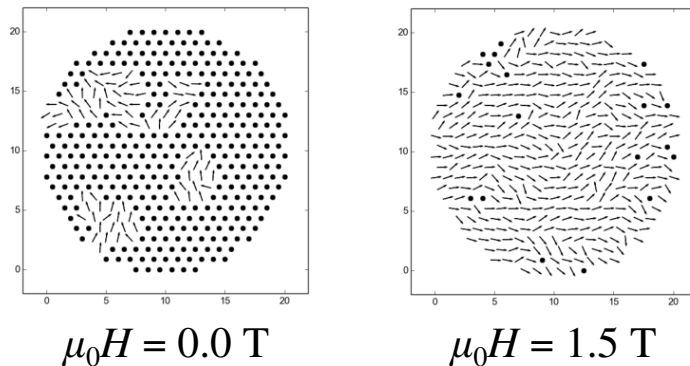


Figure 9. Snapshots of simulated samples at  $kT_{\text{sim}} = 1.0 J$ ,  $E_{\text{AFM}} = -4.2 J$  (see eqs. 10 and 9) in two different states of magnetization: one dominated by AFM clusters (dots) with a low magnetization (left), and one where the clusters are predominantly FM (thin arrows) and the magnetization is high (right). The roughly corresponding magnetic fields (directed towards 3 o'clock in the figure) are indicated below the samples. The distance scales along the edges of the samples are in units of cluster diameters, which could be of order 10 nm in the real world [5, 6] [P4].

magnetic transitions (MMT) associated with the CMR effect [10, 11]. The starting point is simple: assume that there are two kinds of clusters, FM and AFM, on a two-dimensional triangular lattice (figure 9). Let the FM clusters interact with neighboring FM clusters via the classical 2D Heisenberg Hamiltonian,  $\mathcal{H}_{\text{H}}$  (defined below), and let AFM clusters be non-interacting, but by their mere existence, contribute a negative bias term,  $E_{\text{AFM}}$ , to the total free energy of the system. Then, to evolve the system towards a minimum of free energy, construct a series of MH proposals where one cluster is chosen at random, and given a 50:50 chance of either becoming a FM cluster with a randomized magnetic moment, or an AFM cluster. Surprisingly enough, these premises are enough to replicate the MMT.

The Hamiltonian of the FM clusters, defined by

$$\mathcal{H}_{\text{H}} = - \sum_i^{N_{\text{tot}}} \sum_j^{N_{\text{n.n.}}} J_{ij} \mathbf{S}_i \cdot \mathbf{S}_j - \mathbf{B}_{\text{ext}} \cdot \mathbf{S}_i, \quad (10)$$

only takes into account the nearest neighbors (n.n.) and the external magnetic

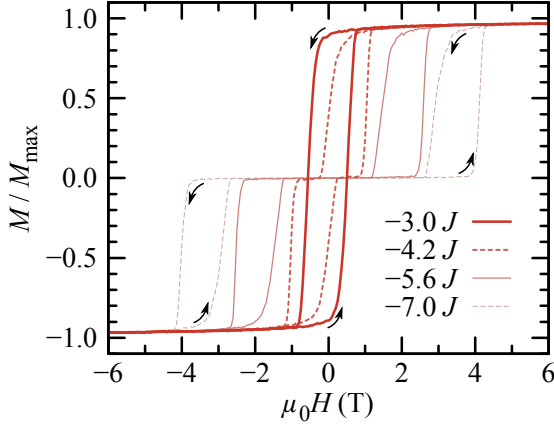


Figure 10. Simulated normalized hysteresis loops at different constant  $E_{\text{AFM}}$  values, at  $kT_{\text{sim}} = 1.0 J$ . As  $E_{\text{AFM}}$  is decreased from  $-3.0 J$  (innermost loop, no MMT) to  $-7.0 J$  (largest MMT fields), the hysteresis loop splits into two metamagnetic subloops along  $H$ . The arrows indicate the direction in which the loops are traced over time.

field, making it computationally very inexpensive to determine the acceptance probability of a given MH proposal. In equation (10), the index  $i$  goes through all  $N_{\text{tot}}$  clusters in the simulated sample, and  $j$  indexes the nearest neighbors of cluster  $i$ , up to  $N_{\text{n.n.}}$ . Due to the imposed triangle lattice geometry (a typical compact packing geometry in 2D),  $N_{\text{n.n.}} \leq 6$ .  $\mathbf{S}_i$  is the magnetic moment of the cluster  $i$  and  $J_{ij}$  the exchange coupling between the clusters  $i$  and  $j$ . In practice,  $J_{ij} = J$  (a global constant) for neighboring FM clusters  $i, j$ , and  $J_{ij} = 0$  otherwise.  $\mathbf{B}_{\text{ext}}$  represents the external magnetic field. By running a series of simulations at different values of the effective temperature,  $T$ , supplied to the Metropolis criterion (equation 9), and the AFM bias energy,  $E_{\text{AFM}}$ , a database of simulated loops can be obtained for quick comparison against experimental data.

Figure 10 shows how the form of the simulated  $M(H)$  loop changes with  $E_{\text{AFM}}$ . In the actual simulations performed for this thesis, lattices of ca. 4000 clusters were modeled in a campaign that took roughly one week to run on a single 3.2GHz desktop CPU core. The simulation software, written in C++ relying only on the standard libraries, was designed to be small enough to run entirely in static memory as a background process.

The mapping of the simulated  $M(H)$  curves to experimental data turns out

to have one major complication: the experimental data must necessarily be interpreted as a superposition of signal from several (probably spatially distinct) environments associated with different values of  $E_{\text{AFM}}$ . To facilitate doing this in an automated and reproducible manner, a graphical least-squares optimizer program was written for the task using the SLSQP optimizer subroutine [90] as implemented in the `scipy.optimize.minimize` method of the SciPy Python package [91]. The implementation was chosen for its speed, benchmarked against other alternatives provided by SciPy on the actual code, in addition to merits of perceived stability.

The program essentially normalized the experimental data to match the output of the simulations by solving for the maximum magnetization, demagnetizing field and linear background susceptibility. The scaling of the magnetic field axis, on the other hand, was fixed to maintain a correspondence between values of  $E_{\text{AFM}}$  and the observed critical magnetic fields of the MMT. In addition to these parameters and the corresponding pair of experimental and simulated loops, the output of the refinement contained the linear combination weights corresponding to the different values of  $E_{\text{AFM}}$ .

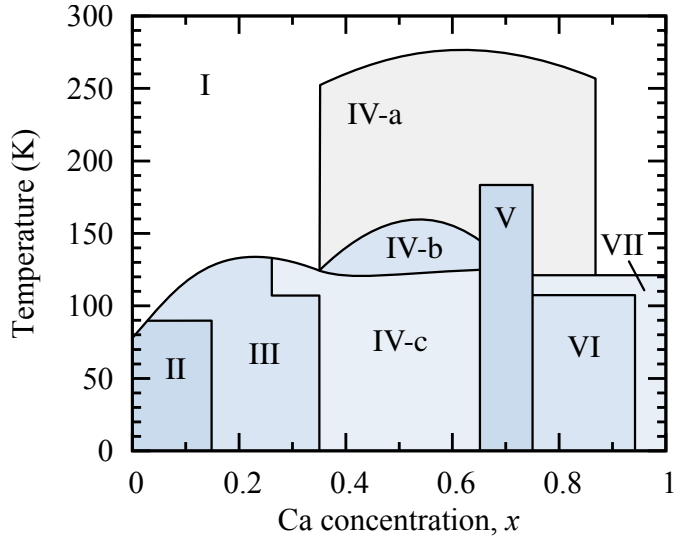


Figure 11. The macroscopic magnetic phase diagram of PCMO. The labeling scheme of the phases is original to this work and bears no physical significance.

## 5 Summary of results

In the following chapters, the results accumulated during the present thesis work will be summarized in two parts. In section 5.1, the nine regions of the macroscopic magnetic phase diagram of PCMO will be described in some detail, highlighting the new findings on the way. Then, in section 5.2, the discussion will zoom in on the microscopic origins of the phase diagram, mapping out, in particular, the prevalence and relevance of magnetic phase separation phenomena.

### 5.1 The macroscopic magnetostructural phase diagram of PCMO

Figure 11 shows a plot of the macroscopic magnetic phase diagram of PCMO [43, 92, 93] [P1] [P3] throughout the accessible range of Ca concentrations,  $x$ . With the knowledge that phase I is just the ordinary paramagnetic (PM) state exhibited by almost all magnetic materials above their ordering temperature [20], one can readily deduce that the magnetofunctionality of PCMO characteristically occurs below room temperature – at least no indications to the contrary appear to have surfaced.

For the following discussion, though mainly given in terms of magnetostructural properties, it is good to remember that the magnetic and electronic properties of PCMO are intimately tied via the DE mechanism. This reservation is necessary, for example, to be able to coherently describe the difference between phases I and IV-a, both being PM in terms of their field dependence of magnetic susceptibility. During the course of this thesis work, at least incremental new results were obtained regarding all phases except for IV-b and VII. The most important advances were arguably made in the description of phases II and IV-c. The following treatment will proceed one phase at a time. The  $x$  and  $T$  limits provided for each phase should be taken as rough approximations; for the actual limits, please always refer to figure 11.

**Phase I:**  $0.00 \leq x \leq 1.00$ ,  $T \geq 280$  K. In this phase, PCMO is a PM semiconductor with an energy gap that varies from ca. 0.2 eV at  $x \leq 0.4$  to almost zero at  $x \geq 0.5$ . In fact, metallic conductivity has been reported at  $x = 0.8$ . Otherwise the conduction is p-type activated at  $x \leq 0.3$  and n-type activated at higher  $x$  [43]. The structure is orthorhombic throughout the Ca doping range and well described by the space group #62 ( $Pnma$  or  $Pbnm$ ) [17] [P1]. Characteristic Jahn-Teller distortions can already be found around  $Mn^{3+}$  ions at room temperature, explaining e.g. the  $x$  dependence of the unit cell volume [65]. The phase I of PCMO is mainly famous for the first observations of a room temperature *memristive* effect (the dependence of electric resistance on the history of electric current flow) seen in thin films of PCMO  $x = 0.3$  [94] and later found in other manganites as well [95]. New results from this thesis work amount to verifying a previously suspected [43] structural phase separation in the range  $0.7 < x < 1.0$ , possibly a solubility gap between PCMO species at roughly  $x \approx 0.75$  and  $x \approx 1.0$  [P1]. An identical phenomenon was also seen in the closely related (Nd, Ca)  $MnO_3$  (NCMO) system [65].

**Phase II:**  $x \leq 0.15$ ,  $T \leq 90$  K. The average magnetic ground state of phase II has been described as canted A-AFM, with a strong ferromagnetic moment confined to the  $ac$  plane of the  $Pnma$  unit cell [43, 96]. The magnetostructure of this phase was studied extensively in [P4] by neutron diffraction, SQUID magnetometry and *ab initio* calculations, and the previously reported type of magnetic ordering was indeed confirmed: at 5 K, there are two magnetic Mn

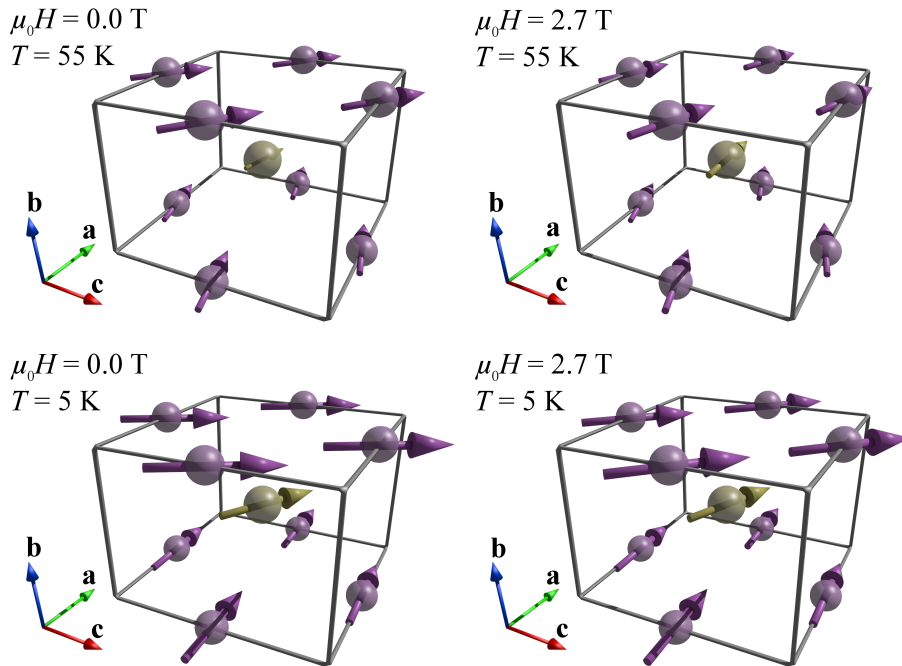


Figure 12. The average magnetic structures found in PCMO  $x = 0.1$  (an example of phase II) by neutron diffraction [P4]. The oxygen atoms are omitted and only a half of the magnetic unit cell is shown along  $c$  for clarity. The coordinate axes correspond to the  $Pnma$  unit cell. The purple arrows on the edges of the cells represent Mn magnetic moments, the yellow ones in the middle stand for the Pr moment. The scaling of the arrows represents the magnitudes of the magnetic moments, but Mn moments should not be visually compared to Pr due to the use of different scaling factors for the elements.



sublattices, both of which are internally FM-coupled in the  $ac$  planes and AFM-coupled along  $c$ . No deviation of the Mn or Pr moments from the  $ac$  plane was observed. As a new result, the study [P4] also found that the magnetic field response of phase II could be approximately modeled by picturing a counter-rotation of the FM planes, as depicted in figure 12.

It should be emphasized that despite the AFM correlations along  $c$ , the saturation magnetization of phase II is very high, ca.  $5.4 \mu_B/\text{FU}$  (Bohr magnetons per  $\text{Pr}_{1-x}\text{Ca}_x\text{MnO}_3$  formula unit), corresponding to an almost total FM alignment of both the Mn and Pr magnetic moments (theoretically  $3.9 \mu_B/\text{FU}$  and  $1.8 \mu_B/\text{FU}$ , respectively) [P4]. The  $M(H)$  curves suggest a rather ordinary soft ferromagnetic behavior [17]. It was therefore a slight surprise when evidence was found for diffracting domains whose size was of order 20 nm in the absence of any magnetic field. The size grew closer to  $1 \mu\text{m}$  when the field was applied, but returned back to nanoscale once the field was lifted. Factoring in the rather large observed magnetostriction and the computationally verified instability of the pure A-AFM structure towards a pure FM structure, the results of [P4] constitute a reasonable argument for extending the AFM-FM phase separation description of the magnetostructure of PCMO down to this exceptionally low Ca concentration. Section 5.2 will elaborate on this point.

While mainly concentrating on the Mn spin system, [P4] also uncovered that the ordered magnetic moment of the Pr ions was significantly higher than previously thought at low temperatures – closer to the full  $1.8 \mu_B/\text{FU}$  instead of just  $0.5 \mu_B/\text{FU}$  at 5 K [43]. Other significant results regarding phase II include the fact that its entropy-based MCE estimate was the best across the whole PCMO family, with  $\mathcal{RC} \approx 370 \text{ J/kg}$  and  $|\Delta S_{\text{max}}| = 4.1 \text{ J/kgK}$  at  $T = 100 \text{ K}$ . The  $\mathcal{RC}$  value closely matches the estimates for some of the best Gd-based magnetocaloric alloys [P3]. The magnetocaloric performance estimates of PCMO are summarized throughout the  $x$  range in figures 13 (transition temperature ranges) and 14 (entropy-based MCE figures of merit).

**Phase III:**  $0.15 \leq x \leq 0.35$ ,  $T \leq 110 \text{ K}$ . This is the FM insulator phase [97], one of the hallmarks of low BW magnanites and a bit of a mystery since the DE interaction would be expected to universally favor metallic conductivity in FM manganites [4–6]. The present thesis did not directly probe phase III in any detail, but one may infer from the results regarding phase II [P4] that the

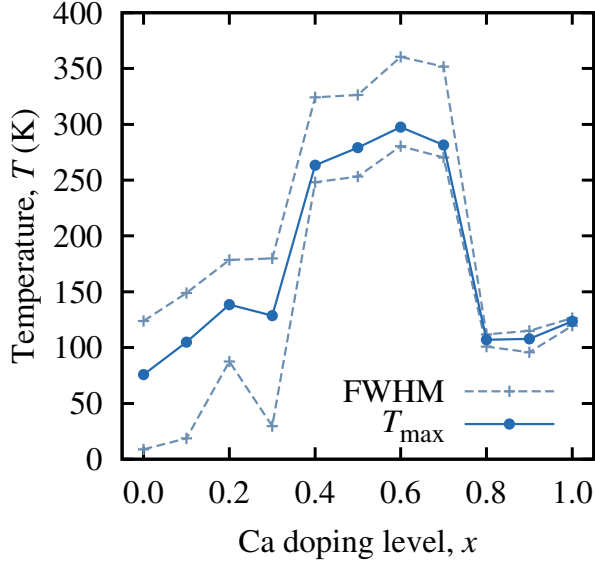


Figure 13. The temperatures of maximum magnetic entropy change,  $T_{\max}$ , vs. the Ca doping level,  $x$ , of PCMO. The dashed lines delimit the FWHM of the corresponding peaks in  $-\Delta S(T)$  [P3].

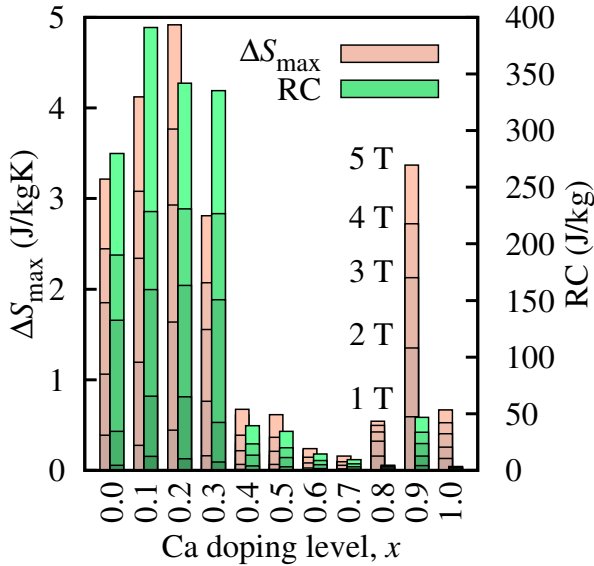


Figure 14. Experimental entropy-based estimates for the MCE in PCMO: magnetic transition entropies,  $\Delta S_{\max}$ , and refrigerant capacities, RC, vs. the Ca doping level,  $x$ . The full  $\Delta S_{\max}$  and RC bars depict the performance of spherical samples in an external field of 5 T. The subdivisions of the bars correspond to lower external fields at intervals of 1 T [P3].

magnitude of the ordered Pr magnetic moment may again have been underestimated in the previous literature [43]. This has implications on the applicability of the phase separation model to explain the insulating electrical behavior, please see the discussion in section 5.2. The magnetocaloric  $\mathcal{RC}$  values of PCMO were generally good in phase III: PCMO  $x = 0.2$  was the second-best within the entire  $x$  range with 340 J/kg, corresponding to a transition with  $|\Delta S_{\max}| = 4.9$  J/kgK at  $T = 140$  K (see figures 13 and 14). PCMO  $x = 0.3$  also came very close with respect to  $\mathcal{RC}$ , even though its  $|\Delta S_{\max}| = 2.9$  J/kgK was considerably lower [P3]. As for almost all phases of PCMO, the structure is  $Pnma$  orthorhombic.

**Phase IV-a:**  $0.35 \leq x \leq 0.85$ ,  $160 \text{ K} \leq T \leq 280 \text{ K}$ . This phase is characterized by the onset of charge ordering (CO) and orbital ordering (OO), the prerequisites of the CMR effect [5, 83, 98–100]. Indeed, applying a sufficient magnetic field (of order 10 T) on PCMO in phase IV-a will lead to a sudden drop in resistivity, even though the full extent of the CMR is not yet realized at these high temperatures [10, 11]. At  $x \geq 0.5$  where phase I showed almost metallic conductivity, phase IV-a can be distinguished by a transition into n-type activated semiconductivity. At  $x \approx 0.4$ , the phase boundary is characterized by the change of conductivity from n-type to p-type.

The magnetic structure of phase IV-a is an intriguing one: the  $M(T)$  curve (figure 15) shows a peak at the border of phases I and IV-a, but measure the  $M(H)$  curve anywhere in this region, and the result will be a straight line. So phase IV-a is PM like phase I, but with an enhanced magnetic moment within the transition region. How this is possible can be understood by analyzing the exchange interactions present in the CE-AFM structure, which is developed in phase IV-b, upon further cooling [5, 101–104].

In anticipation of the CE-AFM ordering, when phase I is cooled down towards phase IV-b (or V or VI, where the anomaly is weaker) through IV-a, the magnetic interactions within the  $ac$  plane of the crystal structure will first cause some of the Mn spins to condense into loosely coupled ferromagnetic chains that dynamically break and reform, generating a randomly fluctuating pattern of PM "macrospins" with a few Mn ions per chain. Indeed, fitting the Curie–Weiss law,  $\chi = C/(T - T_{\text{div}})$ , to the phase I  $M(T)$  curve at the Ca concentrations where phase IV-a is possible will yield a positive divergence

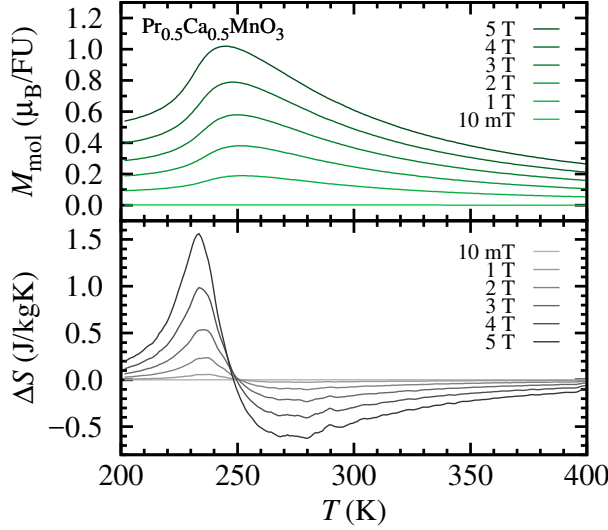


Figure 15. The  $M(T)$  and  $\Delta S(T)$  curves of PCMO  $x = 0.5$  in the vicinity of the CO/OO-related magnetization peak at the border between phases I and IV-a ( $T \approx 250$  K).

temperature,  $T_{\text{div}}$ , for the magnetic susceptibility,  $\chi$  [6], corresponding to dominantly FM exchange interactions [20]. Towards the border between the phase IV-a and one of the lower temperature phases, however, the AFM interactions become strong enough to couple neighboring FM chains antiparallel to each other, rapidly dropping the observed PM moment upon further cooling, thus producing a transient peak in  $M(T)$  [5, 101–104].

For the present thesis, the magnetic structure of phase IV-a was not studied in any detail – it is admittedly difficult to approach theoretically. However, the structural analysis reported in [P2] uncovered that a transient increase in crystal volume also accompanies the  $M(T)$  anomaly at the border between phases I and IV-a (figure 16). This was attributed to additional structural disorder due to DE-mediated OO fluctuations during the "FM chain" phase. Upon further cooling, a continuous orthorhombic-to-monoclinic transition occurs as suggested by the earlier literature [105–107], changing the space group from  $Pnma$  to  $P2_1/m$ . Although the magnetic transition between phases I and IV-a occurs conveniently close to the room temperature, the entropy changes associated with it (see figures 13 and 14) are, unfortunately, too small for magnetocaloric applications [P3].

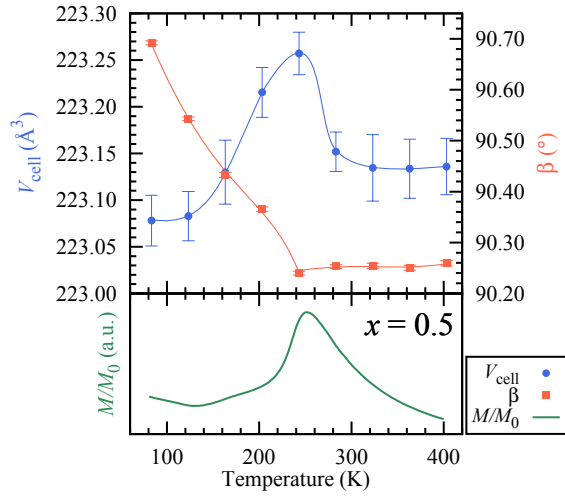


Figure 16. The unit cell volume,  $V_{\text{cell}}$ , monoclinic cell angle,  $\beta$ , and normalized magnetization,  $M/M_0$ , as functions of temperature for PCMO  $x = 0.5$ . The solid lines connecting the  $V_{\text{cell}}$  and  $\beta$  data points provide a guide for the eye. A transient increase of  $V_{\text{cell}}$  is observed coincident with the magnetic CO/OO anomaly. The error bars are based on standard deviations calculated by FullProf [79], composed by the total differential approximation for  $V_{\text{cell}}$ . The line width exceeds the error in  $M/M_0$ .

**Phase IV-b:**  $0.35 \leq x \leq 0.65$ ,  $120 \text{ K} \leq T \leq 160 \text{ K}$ . In this phase, PCMO shows the least distorted CE-AFM structure possible for any given Ca concentration,  $x$  [43]. At  $x = 0.5$ , the perfect CE-AFM can indeed be found alongside the "checkerboard" CO/OO pattern (figure 7) [5, 6]. Towards lower values of  $x$  the magnetic moments will somewhat twist away from the  $ac$  plane, though they still retain an approximately zero net magnetization [43]. It is likely that the CO pattern simultaneously shifts from the totally site-centered configuration of  $x = 0.5$  to a partially bond-centered one, implying the valences of Mn ions may no longer be treated as integers [28]. At  $x > 0.5$ , there are, unfortunately, more questions than answers regarding the spatial arrangement of the CO [6]. The magnetic structure at  $x = 0.6$  is reportedly highly similar to  $x = 0.4$  [43], though the general phase diagram suggests  $C_xE_{1-x}$  as a possible alternative solution [53, 55]. No new results regarding phase IV-b were obtained during this thesis work. The crystal structure is  $P2_1/m$  monoclinic, inherited from phase IV-a.

**Phase IV-c:**  $0.35 \leq x \leq 0.65$ ,  $T \leq 120 \text{ K}$ . This is arguably the technologically most relevant phase of PCMO – the magnitude of the CMR effect is at its maximum, although so are the associated critical magnetic fields,  $\mu_0 H_{\text{MMT}}$ , often reaching over 12 T [10, 11, 18]. The magnetostructure is otherwise similar to phase IV-b [43], but a spontaneous FM component is developed regardless of  $x$  [17] [P1]. The crystal structure remains  $P2_1/m$  monoclinic. The study [P5], aimed at modeling the mechanism of the CMR effect, was exclusively conducted within phase IV-c. An extended discussion on the results will be given in section 5.2 in terms of the FM–AFM phase separation framework, but to summarize, it was found that  $\mu_0 H_{\text{MMT}}$  is highly dependent on the geometry of the sample. In particular, based on comparisons between microcrystalline, nanocrystalline and thin film samples,  $\mu_0 H_{\text{MMT}}$  is almost universally minimized when the smallest spatial dimension of the sample approaches 100 nm and the elastic strain is minimized. When these conditions are met,  $\mu_0 H_{\text{MMT}}$  is brought down to a relatively accessible value of 3 T at around 70 K [P5], with room for even more improvement in case optical illumination can be applied [9].

**Phase V:**  $0.65 \leq x \leq 0.75$ ,  $T \leq 180$  K. Despite the the considerable departure from half doping ( $x = 0.5$ ), phase V reportedly retains an OO structure similar to phase IV-b, justifying the extension of phase IV-a across both (figure 11). Due to the significantly lower occupation of the Mn  $3d e_g$  orbitals in phase V, however, the OO is not quite as robust, and also the related magnetic anomaly at the border between phases I and IV-a is much weaker at  $x \geq 0.7$  [P1]. Correspondingly, the magnetic structure of phase V is quite far from the ideal CE pattern. In fact, it is reportedly helimagnetic, a superposition of two C-AFM spin arrangements that evolve along the  $a$  axis of the  $Pnma$  unit cell with a period of ca.  $35 \text{ \AA}$  [43]. No major new discoveries were made regarding phase V during this thesis work.

**Phase VI:**  $0.75 \leq x \leq 0.95$ ,  $T \leq 110$  K. Phase VI is sometimes referred to as the optimal electron doping region. The electron band gap fluctuates very close to zero, reportedly vanishing altogether at  $x \approx 0.8$  to yield metallic conductivity. The magnetic structure of the phase is C-AFM [43]. Around  $x \approx 0.9$ , PCMO (like other low BW manganites) also shows an interesting, narrow region where the magnetic structure develops a FM component, and large magnetoresistance ratios can be observed [92, 108]. For PCMO  $x = 0.865$ , an optimal ratio of 400 has been reported between the resistivities measured at zero field and at  $\mu_0 H = 7$  T at 5 K [108]. Though not insignificant, this number pales in comparison with the magnitude of the CMR effect at  $x \approx 0.4$ , where ratios in excess of  $10^7$  are standard [9]. Even so, the glassy properties [92, 108] of the FM structure that suddenly emerges within phase VI should provide interesting material for e.g. future *ab initio* models that could perhaps be constructed via small perturbations of the  $x = 1.0$  parent material,  $\text{CaMnO}_3$ . Phases VI and VII share an almost tetragonal  $Pnma$  unit cell symmetry.

The present thesis work did not place a heavy focus on phase VI, because it was found to be afflicted by a structural phase separation [P1]. The two thermodynamically stable phases were chemically too similar to be conclusively identified by XRD (diffractogram in figure 17), but an educated guess might describe the situation as a solubility gap between PCMO phases at Ca concentrations close to  $x \approx 0.75$  and  $x \approx 1.0$ . Such a phase separation had already been suggested by earlier neutron diffraction work on PCMO [43], and an identical problem is known to arise in the NCMO system [65]. The two

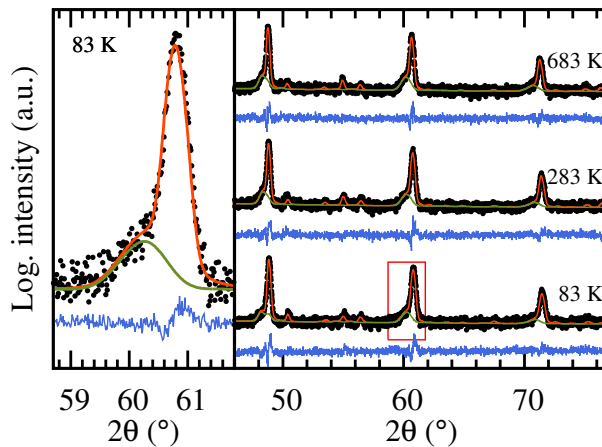


Figure 17. XRD Rietveld refinement plots of diffractograms of PCMO  $x = 0.9$  at different temperatures, portraying the structural phase separation. The panel on the left gives a detail of the PCMO peak group (240)(321) at 83 K, which is also highlighted on the right. The measured data (black dots) are overlaid with two fit curves: the total PCMO fit (orange), and the contribution from the minority phase (shoulders to the lower- $2\theta$  side of all peaks, green). The intensities are drawn on a logarithmic scale to accentuate the low-intensity minority phase, which also leads to a visual exaggeration of the background noise. Difference curves between the total fit and the observed intensity are shown on a linear scale below each diffractogram [P1].



structural phases support different magnetic structures, only one of which actually corresponds to the C-AFM arrangement described above. The other, with a slightly higher ordering temperature, is highly similar to the G-AFM structure of phase VII, supporting the solubility gap interpretation [43] [P1]. This is the reason why phase VII is portrayed completely enveloping phase VI from the higher-temperature side in figure 11, even though additional neutron diffraction work would certainly be in order to rigorously justify this particular detail.

**Phase VII:**  $x \geq 0.95$ ,  $T \leq 120$  K. Phase VII inherits the distorted G-AFM magnetic structure of the  $x = 1.0$  parent compound,  $\text{CaMnO}_3$  [41, 43, 54]. An objective comparison among the phase VII PCMO species can be somewhat difficult due to the fact that these materials can readily form with various degrees of oxygen understoichiometry depending on the sintering conditions, which in turn heavily influences the magnetic structure by modifying the Mn valence. Via what can be described as the canting of the spin sublattices of the G-AFM structure, phase VII develops a hard FM component if any  $\text{Mn}^{3+}$  is present [39–43, 54] [P1]. Within the scope of the present thesis work, phase VII mainly acted as an undesirable complication to the analysis of phase VI (see above), and was not given a particular research priority, in part because obtaining a phase pure sample was found to require a somewhat cumbersome (and potentially dangerous) final sintering in a 100% oxygen atmosphere [P1]. The parent compound  $\text{CaMnO}_3$  can nowadays be seen to attract greater interest within the field of catalytical chemistry than among condensed matter physicists, as the material is being tested for e.g. the production of biodiesel [109] and various applications of electrocatalysis [110]. Thanks to the almost complete absence of cooperative JT distortions (see section 1.2) the perovskite unit cell is practically cubic, but for compatibility with other manganite studies, the less symmetric  $Pnma$  orthorhombic description is often used.

## 5.2 The role of dynamic nanoscale phase separation in PCMO

With such a number of experimentally accessible macroscopic phases popping up, it is fair to ask whether we could simplify our description of PCMO by explaining the macroscopic properties as being emergent from the interactions among a smaller number of microscopic phases – perhaps just two, one FM

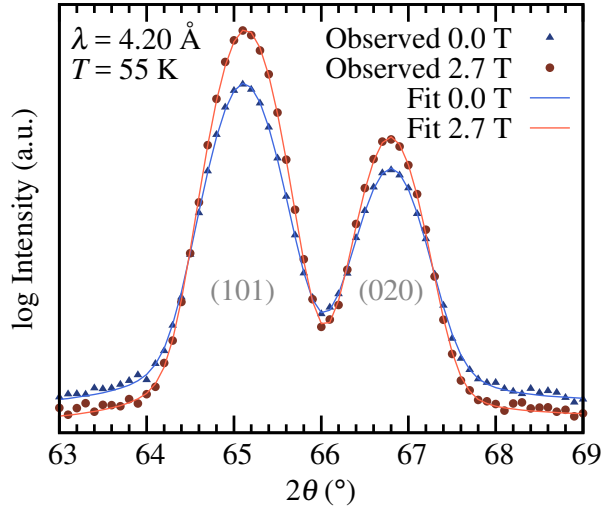


Figure 18. The effects of a 2.7 T applied magnetic field on the profiles of the magnetic Bragg reflections (101) and (020) of PCMO  $x = 0.1$ . The graph consists of cold neutron diffraction datasets measured at  $T = 55$  K,  $\lambda = 4.20$  Å and the respective pseudo-Voigt sum profiles obtained by Levenberg–Marquardt fits [111]. The 0.0 T peaks are observably broadened at their base by diffracting domain size effects interpreted to signify the presence of nanoscale magnetic clusters.

and the other AFM [5, 6]. The role of the present section is to build up a largely affirmative answer to that question.

The present thesis work admittedly suffers from the lack of methodology suitable for directly imaging microscopic magnetic phenomena, but fortunately, the cold neutron diffractometry exercised in [P4] comes close to fulfilling this need. The method has a very high  $d$  resolution at the low diffraction vector magnitudes (high  $d$  values) where the magnetic Bragg reflections are most intense, allowing one to extract detailed information on the distribution of the magnetic diffracting domains. Thus, when 20 nm magnetic clusters were observed by this method (based on the "tails" of the Bragg reflections seen in figure 18), and the accompanying results regarding measured magnetostriction and calculated magnetic phase stabilities supported the presence of both FM and AFM phases at the same time, it arguably became more plausible to describe PCMO  $x = 0.1$  as a phase mixture than as a rather extremely canted A-type antiferromagnet [P4]. Similar conclusions have been reached on the

analogous NCMO system [112, 113].

To be able to extend the phase separation description outside of the optimal doping region, ca.  $0.3 \leq x \leq 0.6$ , where it was originally formulated to explain the CMR effect [5, 6], actually has several consequences. In particular, this result clarifies the driving force behind any such phase separation – it is not the electronic CO phenomenon (that only occurs near  $x = 0.5$ ), but the OO and the associated structural modulations present almost throughout the Ca doping range that most basically determine the FM–AFM equilibrium. Previously published computational models [21], as well as the one developed as a part of this thesis [P5], concur with that picture.

Also, if a FM–AFM phase separation is present at  $x = 0.1$  [P5] and  $x = 0.3$  [13], then why not at  $x = 0.2$ , where it could elegantly explain the insulating character of the almost completely FM material, without discrediting the otherwise useful DE heuristic? The main argument published against this view appears to be that the ground state ordered magnetic moment, reportedly about  $2 \mu_B$ , would suggest a FM phase concentration well above the percolation threshold [97]. The implication would certainly be true if the magnetic moment was entirely produced by Mn spins, but based on our findings on the magnetic role of Pr at  $x = 0.1$  [P4], it is reasonable to believe that a considerable part of the  $2 \mu_B$  is in fact due to unaccounted Pr spins, and PCMO  $x = 0.2$  can be below the FM percolation threshold after all.

With the above taken into consideration, we can see that the FM–AFM phase separation framework carries a high explanative power across more than half of the magnetic phase diagram of PCMO, from  $x = 0.0$  to at least  $x = 0.6$ , and even further with some reservations, since remnants of phase IV-a (the CO onset phase with OO similar to  $x = 0.5$ ) can be found up to  $x = 0.8$  [P1]. In such a situation, it is well justified to try and develop more predictive models that incorporate the explanative framework. The contribution of the present thesis work towards that goal is reported in [P5].

Though developed to describe the dependence of the critical magnetic field,  $\mu_0 H_{\text{MMT}}$ , of the CMR-related MMT on the sample geometry, the dynamic mesoscale model of [P5] (also described in section 4.2) does not explicitly rely on the presence of CO – this particular electronic structure is only required for the CMR effect to be possible. Indeed, one can compare the simulated  $M(H)$  loops in figure 10 with the published experimental hysteresis data of PCMO

and NCMO at  $x \approx 0.1$ , far from the CMR region [17, 113], and still see a fair resemblance. This is another indication of the prevalence of similar magnetic phase separation dynamics throughout the majority of the Ca doping range.

To better describe the similarity of the phase separation dynamics between Ca concentrations, figure 19(a) shows measured  $M(H)$  loops of bulk PCMO  $x = 0.4$  (B4) and PCMO  $x = 0.5$  (B5) overlaid with the corresponding simulated data. One of the conjectures of the model [P5] is that the hysteretic part of the loops is completely described by an effective temperature,  $T_{\text{sim}}$ , and the distribution of the AFM state bias energies,  $n(E_{\text{AFM}})$  (figure 19(b)), that can be likened to the distribution of  $\mu_0 H_{\text{MMT}}$  (though the correspondence is not trivial). Granted, the model requires a lot of calibration to be of any predictive use, but on the other hand, it shows that the interactions between FM clusters can roughly be described by a single scalar constant,  $J$ , hiding all of the atom-scale complexity into  $n(E_{\text{AFM}})$ , which, on the other hand, can be determined experimentally at key points in the phase space to establish a calibration. The interactions are surprisingly insensitive to  $x$  (see figure 19(a)), although some reservations must probably be made for situations where one of the macroscopic phase boundaries found in figure 11 needs to be crossed by the model.

The  $n(E_{\text{AFM}})$  data output by the model for each  $M(H)$  loop can be refined to yield a scalar quantity  $n_{\text{FM}}$ , the relative concentration of permanently FM hysteretic clusters, which turns out to trace a curve specific to the sample geometry when plotted against the temperature (figure 20). Though the amount of experimental data on the subject is still limited, it seems clear that at least in the absence of applied elastic stress<sup>5</sup>, the FM phase is favored over the AFM phase when the sample geometry is characterized by a high surface-to-volume ratio [73].

With a little leap of faith, one could arguably pin the fundamental difference between the bulk-like samples (B4 and B5 in figure 20) and the dimensionally confined samples to the maximum spatial extent through which a coherent three-dimensional OO is possible – the large crystallites of the bulk samples are able to support coherence lengths of order 1000 nm in all directions, consistently yielding  $n_{\text{FM}} \leq 0.4$ , whereas in the other samples, the coherence length is geometrically limited to 100 nm or less, and  $n_{\text{FM}} \geq 0.4$ . To arrive at a more

---

<sup>5</sup>Note that when the minimum sample dimension falls below 100 nm, additional elastic strain may well develop e.g. due to film–substrate interactions [114] or surface reconstruction effects [73]. Strain is known to heavily influence the AFM–FM equilibrium [21, 57].

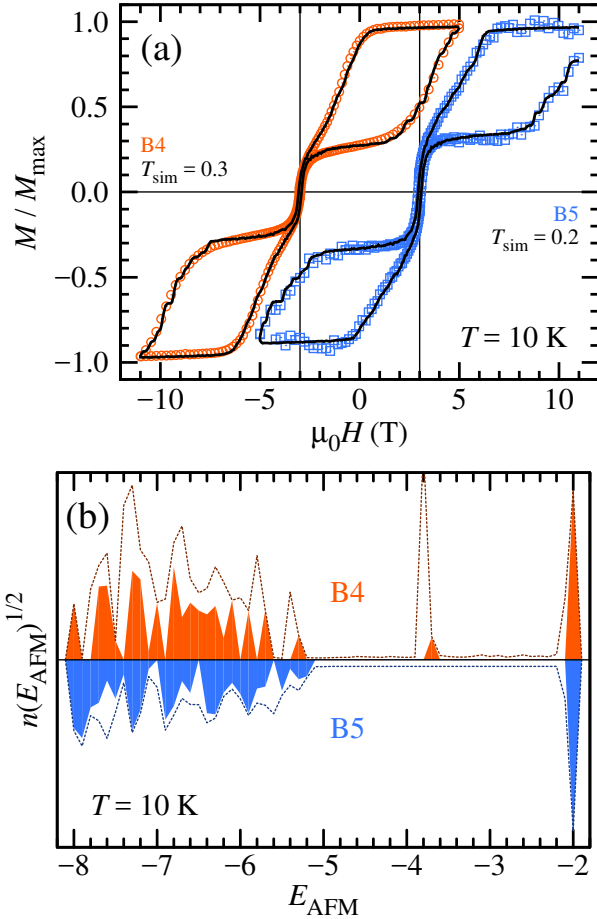


Figure 19. Hysteresis loops of bulk PCMO samples at  $T = 10$  K, normalized to the simulated form (a) and the distribution of  $E_{\text{AFM}}$  (b) extracted from these loops. In (a), the light open dots and boxes correspond to measured data (B4 or PCMO  $x = 0.4$  and B5 or PCMO  $x = 0.5$ , respectively) and the solid black lines to simulated data. The origins of the loops have been shifted for clarity. In (b), the number densities of the clusters at each  $E_{\text{AFM}}$  (outlines of the solid colored regions) increase upwards for B4 and downwards for B5. The dark dashed lines delimit the maximal fluctuations of the parameters if the total square error is allowed to increase by 1%.

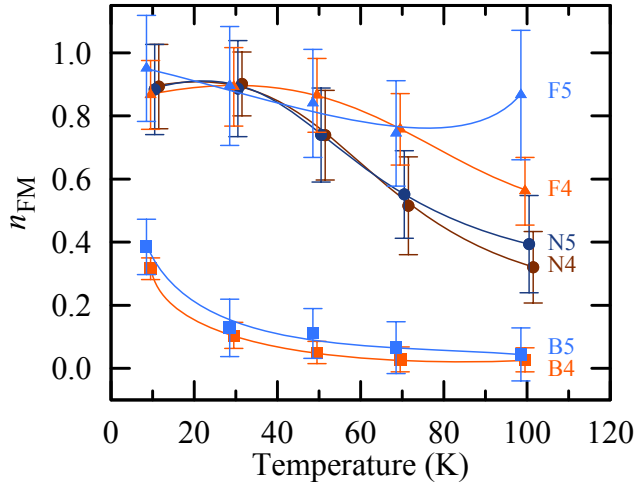


Figure 20. Relative concentrations of permanently FM hysteretic clusters,  $n_{\text{FM}}$ , in different phase IV-c PCMO samples vs. the temperature [P5]. The samples B4/5 are microcrystalline powders (PCMO  $x = 0.4$  and PCMO  $x = 0.5$ , respectively; crystallite size ca. 1000 nm), N4/5 nanoparticles (size ca. 40 nm) and F4/5 thin films (thickness ca. 100 nm). The errors correspond to maximal parameter shifts compatible with allowing the square error of the underlying fits to increase by 1% (see figure. 19). The data points have been shifted by increments of 1 K along the temperature axis to contrast individual error bars. The solid curves connecting the data points are a guide for the eye.

precise correspondence, and to further test the meaningfulness of the model in general, it would be a straightforward continuation to develop the sintering process of PCMO towards a better-controlled grain morphology (in this thesis work, only chemical purity and average crystallite size were given any significance) and establish a solid link between the sample morphology and the simulation parameters,  $T_{\text{sim}}$  and  $n(E_{\text{AFM}})$ , at different experimentally accessible points on the  $(x, T)$  plane. At the same time, the model could be amended to e.g. predict the linear magnetic susceptibility of the AFM phase for a complete description of the measured  $M(H)$  data, and perhaps more importantly, a resistor network simulation of the CMR effect could be implemented for comparison with experiments [57].

## 6 Conclusions

The objective of this thesis has been to offer the reader an abstract map to the macroscopic magnetic phase diagram of PCMO, and to outline the set of microscopic phenomena and mechanisms from which the observable large scale properties can be understood to emerge. For the majority of the accessible Ca doping range, microcrystalline PCMO could be synthesized in a simple and efficient manner using the ceramic solid state method, yielding highly crystalline samples for reliable diffractometric characterization. Problems in this regard only arose at the highest of Ca concentrations, at  $x \geq 0.8$ , where a verified structural phase separation and a thermodynamical preference for oxygen understoichiometry complicated the analysis [P1]. For a better control of crystallite morphology, sol-gel autocombustion synthesis was also briefly visited [P5].

At  $x \leq 0.8$ , a coherent picture of the magnetic phase diagram could be established in terms of the FM–AFM phase separation framework. Though originally conceived in order to explain the CMR effect at  $0.3 \leq x \leq 0.5$ , the framework was found to carry a significant amount of explanative power also outside of this canonical Ca doping range. In particular, with the help of cold neutron diffractometry, SQUID magnetometry and *ab initio* simulations, the presence of a FM–AFM phase separation was verified at  $x = 0.1$  [P4]. Along with that, another finding regarding the role of Pr spins helped cross the gap from the magnetic structure at  $x = 0.1$  to the one at  $x = 0.3$ , offering a revised explanation for the FM insulating behavior of PCMO  $x = 0.2$  in better harmony with contemporary results throughout the Ca doping range.

After observing an anomalous thermal expansion phenomenon related to the phase separation mechanism [P2], a dynamic mesoscale model of the mechanism was constructed to verify and study its sensitivity to sample geometry [P5]. The FM component of the phase equilibrium was found to preferentially nucleate at crystallite interfaces, allowing one to tune the critical magnetic field of the MMT associated with the CMR by geometrical design choices. The field could be consistently minimized to roughly 3 T by bringing the smallest spatial dimension of the sample close to 100 nm while minimizing external elastic stresses at the same time. Natural continuation pathways for the physical characterization of PCMO could be suggested in terms of the model – in particular, the approach should readily be able to incorporate a resistor network simu-



lation of the CMR effect that could be directly compared with experimental results.

As a natural byproduct of characterizing the magnetic transitions of PCMO, entropy-based estimates for the magnetocaloric applicability of the material family were also obtained. In this regard, PCMO turns out to mainly suffer from the fact that its magnetic transitions occur far from room temperature, since at around 100 K, the refrigerant capacity estimates place PCMO on par with some of the best Gd-based magnetocaloric alloys [P3].

## References

- [1] T. Hyodo *et al.*, Journal of applied electrochemistry **27**, 745 (1997).
- [2] T. Arakawa, A. Yoshida, and J. Shiokawa, Mater. Res. Bull. **15**, 269 (1980).
- [3] J.M.D. Coey, M. Viret, and S. von Molnár, Adv. Phys. **58**, 571 (2009).
- [4] M.B. Salamon and M. Jaime, Rev. Mod. Phys. **73**, 583 (2001).
- [5] E. Dagotto, T. Hotta, and A. Moreo, Phys. Rep. **344**, 1 (2001).
- [6] E. Dagotto, *Nanoscale phase separation and colossal magnetoresistance: the physics of manganites and related compounds* (Springer Science & Business Media, 2013), Vol. 136.
- [7] J. Fontcuberta *et al.*, Phys. Rev. Lett. **76**, 1122 (1996).
- [8] A.-M. Haghiri-Gosnet and J.-P. Renard, J. Phys. D: Appl. Phys. **36**, R127 (2003).
- [9] T. Elovaara, S. Majumdar, H. Huhtinen, and P. Paturi, Adv. Funct. Mater. **25**, 5030 (2015).
- [10] M. Tokunaga, N. Miura, Y. Tomioka, and Y. Tokura, Phys. Rev. B **57**, 5259 (1998).
- [11] M. Respaud *et al.*, Phys. Rev. B **61**, 9014 (2000).
- [12] P. Beaud *et al.*, Nat. Mater. **13**, 923 (2014).
- [13] D. E. Cox, P. G. Radaelli, M. Marezio, and S-W. Cheong, Phys. Rev. B **57**, 3305 (1998).
- [14] A. Asamitsu, Y. Tomioka, H. Kuwahara, and Y. Tokura, Nature **388**, 50 (1997).
- [15] K. Raju, G. Lalitha, K.V. Sivakumar, and P. Venugopal Reddy, Solid State Commun. **150**, 928 (2010).
- [16] D.K. Baisnab *et al.*, J. Magn. Magn. Mater. **323**, 2823 (2011).
- [17] T. Elovaara, H. Huhtinen, S. Majumdar, and P. Paturi, J. Phys.: Condens. Matter **24**, 216002 (2012).
- [18] Y. Tomioka *et al.*, Phys. Rev. B **53**, R1689 (1996).
- [19] M. Kumada *et al.*, IEEE Transactions on Applied Superconductivity **14**, 1287 (2004).
- [20] J.M.D. Coey, *Magnetism and magnetic materials* (Cambridge University Press, 2010).
- [21] K. H. Ahn, T. Lookman, and A. R. Bishop, Nature **428**, 401 (2004).
- [22] M. Azhar and M. Mostovoy, Phys. Rev. Lett. **118**, 027203 (2017).
- [23] J. Fidler and T. Schrefl, J. Phys. D: Appl. Phys. **33**, R135 (2000).
- [24] H. Ebert, D. Ködderitzsch, and J. Minár, Rep. Prog. Phys. **74**, 096501 (2011).
- [25] C. Moure and O. Peña, Progress in Solid State Chemistry **43**, 123 (2015).
- [26] C. McCammon, Nature **387**, 694 (1997).

- [27] D. E. Cox *et al.*, Applied Physics Letters **79**, 400 (2001).
- [28] D.V. Efremov, J. van den Brink, and D.I. Khomskii, Nat. Mater. **3**, 853 (2004).
- [29] R.D. Shannon, Acta Cryst. **A32**, 751 (1976).
- [30] C. Moure and O. Peña, J. Magn. Mater. **337–338**, 1 (2013).
- [31] I. Mansuri *et al.*, Journal of Magnetism and Magnetic Materials **323**, 316 (2011).
- [32] J.B. Goodenough, Phys. Review **100**, 2 (1955).
- [33] M.W. Lufaso and P.M. Woodward, Acta Crystallographica Section B **60**, 10 (2004).
- [34] P.M. Woodward, Acta Crystallographica Section B: Structural Science **53**, 32 (1997).
- [35] P.M. Woodward, Acta Crystallographica Section B: Structural Science **53**, 44 (1997).
- [36] J.P. Zhou *et al.*, Applied Physics Letters **75**, 1146 (1999).
- [37] H.S. Lee, S.G. Choi, H.-H. Park, and M.J. Rozenberg, Scientific reports **3**, (2013).
- [38] E. Pollert, S. Krupička, and E. Kuzmičová, J. Phys. Chem. Solids **43**, 1137 (1982).
- [39] L. Rørmark *et al.*, Chem. Mater **13**, 4005 (2001).
- [40] A. Reller, J.M. Thomas, D.A. Jefferson, and M.K. Uppal, Proc. R. Soc. Lond. A **394**, 223 (1984).
- [41] Z. Zeng, M. Greenblatt, and M. Croft, Phys. Rev. B **59**, 8784 (1999).
- [42] H. Taguchi, Physica status solidi (a) **88**, K79 (1985).
- [43] Z. Jiráček *et al.*, J. Magn. Mater. **53**, 153 (1985).
- [44] E.F. Kneller and R. Hawig, IEEE Trans. Magn. **27**, 3588 (1991).
- [45] G.J. Snyder *et al.*, Physical Review B **55**, 6453 (1997).
- [46] J. Kanamori, Journal of Physics and Chemistry of Solids **10**, 87 (1959).
- [47] P.W. Anderson, Phys. Rev. **115**, 2 (1959).
- [48] L.E. Gontchar and A.E. Nikiforov, Phys. Rev. B **66**, 014437 (2002).
- [49] C. Zener, Physical Review **81**, 440 (1951).
- [50] Y. Murakami *et al.*, Nat. Nanotechnol. **5**, 37 (2010).
- [51] H. Gamari-Seale *et al.*, Physica B: Condensed Matter **350**, E19 (2004).
- [52] I.O. Troyanchuk, S.N. Pastushonok, O.A. Novitskii, and V.I. Pavlov, J. M. M. **124**, 55 (1993).
- [53] R. Kajimoto, H. Yoshizawa, Y. Tomioka, and Y. Tokura, Phys. Rev. B **66**, 180402 (2002).
- [54] E.O. Wollan and W.C. Koehler, Phys. Rev. **100**, 545 (1955).
- [55] T. Hotta, Y. Takada, H. Koizumi, and E. Dagotto, Phys. Rev. Lett. **84**, 2477

- (2000).
- [56] M. Uehara, S. Mori, C. H. Chen, and S.-W. Cheong, *Nature* **399**, 560 (1999).
- [57] K. Lai *et al.*, *Science* **329**, 190 (2010).
- [58] G.C. Milward, M.J. Calderon, and P.B. Littlewood, *Nature* **433**, 607 (2005).
- [59] V. Franco, J.S. Blázquez, B. Ingale, and A. Conde, *Annu. Rev. Mater. Res.* **42**, 305 (2012).
- [60] E. Brück, *J. Phys. D: Appl. Phys.* **38**, R381 (2005).
- [61] K.A. Gschneidner Jr, V.K. Pecharsky, and A.O. Tsokol, *Reports on Progress in Physics* **68**, 1479 (2005).
- [62] J. Romero Gómez, R. Ferreiro Garcia, A. De Miguel Catoira, and M. Romero Gómez, *Renewable and Sustainable Energy Reviews* **17**, 74 (2013).
- [63] M.H. Phan and S.-C. Yu, *J. Magn. Magn. Mater.* **308**, 325 (2007).
- [64] G. Wang, Ph.D. thesis, Universidad de Zaragoza, 2012.
- [65] A. Beiranvand *et al.*, **4**, 036101 (2017).
- [66] A. Stein, S.W. Keller, and T.E. Mallouk, *Science* **259**, 1558 (1993).
- [67] S. Krupička, M. Maryško, Z. Jiráček, and J. Hejtmánek, *J. Magn. Magn. Mater.* **206**, 45 (1999).
- [68] M. Maryško and Z. Jiráček, *Acta Phys. Pol. A* **113**, 143 (2008).
- [69] T. Higuchi *et al.*, *Appl. Phys. Lett.* **95**, 043112 (2009).
- [70] G. B. Song, J. S. Amaral, V. S. Amaral, and A. L. Kholkin, *J. Eur. Ceram. Soc.* **27**, 3941 (2007).
- [71] P.Z. Si *et al.*, *Solid State Commun.* **142**, 723 (2007).
- [72] E.I. Ko, *Preparation of Solid Catalysts* 85 (1999).
- [73] T. Zhang, T. F. Zhou, T. Qian, and X. G. Li, *Phys. Rev. B* **76**, 174415 (2007).
- [74] J. Als-Nielsen and D. McMorrow, *Elements of modern X-ray physics* (John Wiley & Sons, 2011).
- [75] C. Kittel, *Introduction to solid state physics* (John Wiley & Sons, Inc., 2005).
- [76] H.M. Rietveld, *Journal of Applied Crystallography* **2**, 65 (1969).
- [77] W.I.F. David, *J. Res. Natl. Inst. Stand. Technol.* **109**, 107 (2004).
- [78] B.H. Toby, *Powder Diffr.* **21**, 67 (2006).
- [79] J. Rodríguez-Carvajal, *Physica B* **192**, 55 (1993).
- [80] A.C. Larson and R.B. Von Dreele, *General Structure Analysis System (GSAS)*, Los Alamos National Laboratory Report LAUR 86-748, 1994.
- [81] L. Lutterotti, *Material Analysis Using Diffraction 2.71*, <http://maud.radiographema.com> (accessed 5th Dec 2016), 1997–2016.
- [82] L. Lutterotti, *Nuclear Instruments and Methods in Physics Research Section B: Beam Interactions with Materials and Atoms* **268**, 334 (2010).

- [83] M. v. Zimmermann *et al.*, Phys. Rev. Lett. **83**, 4872 (1999).
- [84] P. Hohenberg and W. Kohn, Phys. Rev. **136**, B864 (1964).
- [85] W. Kohn and L.J. Sham, Phys. Rev. **140**, A1133 (1965).
- [86] W. K. Hastings, Biometrika **57**, 97 (1970).
- [87] C.P. Robert, *Monte carlo methods* (Wiley Online Library, 2004).
- [88] S. Kirkpatrick, C.D. Gelatt, and M.P. Vecchi, Science **220**, 671 (1983).
- [89] H.L. Anderson, Los Alamos Science **14**, 96 (1986).
- [90] D. Kraft *et al.*, *A software package for sequential quadratic programming* (DFVLR Obersfaffenhofen, Germany, 1988).
- [91] E. Jones *et al.*, SciPy: Open source scientific tools for Python, 2001–, [Online; accessed 2017-01-16].
- [92] C. Martin, A. Maignan, M. Hervieu, B. Raveau, Phys. Rev. B **60**, 12191 (1999).
- [93] M.S. Reis *et al.*, Phys. Rev. B **71**, 144413 (2005).
- [94] S.Q. Liu, N.J. Wu, and A. Ignatiev, Applied Physics Letters **76**, 2749 (2000).
- [95] D. Rubi *et al.*, Thin Solid Films **583**, 76 (2015).
- [96] Z. Jiráček, S. Vratislav, and J. Zajíček, Phys. Status Solidi A **52**, K39 (1979).
- [97] R. Kajimoto *et al.*, Phys. Rev. B **69**, 054433 (2004).
- [98] Z. Jiráček, C. Martin, M. Hervieu, and J. Hejtmánek, Appl. Phys. A **74**, S1755 (2002).
- [99] Z. Jiráček *et al.*, Phys. Rev. B **61**, 1181 (2000).
- [100] Z. Jiráček *et al.*, Phys. Rev. B **81**, 024403 (2010).
- [101] H. Yang *et al.*, Phys. Rev. B **91**, 174405 (2015).
- [102] M. R. Lees *et al.*, Phys. Rev. B **52**, R14303 (1995).
- [103] N. Biškup, A. de Andrés, and M. García Hernández, Phys. Rev. B **78**, 184435 (2008).
- [104] K. Okada and S. Yamada, Phys. Rev. B **86**, 064430 (2012).
- [105] Y Tokura and Y Tomioka, J. Magn. Magn. Mater. **200**, 1 (1999).
- [106] A. Martinelli *et al.*, Phys. Rev. B **73**, 064423 (2006).
- [107] M. R. Lees *et al.*, Phys. Rev. B **58**, 8694 (1998).
- [108] A. Maignan, C. Martin, F. Damay, and B. Raveau, Chem. Mater. **10**, 950 (1998).
- [109] Ž. Kesić *et al.*, Fuel Processing Technology **143**, 162 (2016).
- [110] X. Han *et al.*, Advanced Materials **26**, 2047 (2014).
- [111] D.W. Marquardt, Journal of the Society for Industrial and Applied Mathematics **11**, 431 (1963).
- [112] V.A. Khomchenko *et al.*, J. Magn. Magn. Mater. **288**, 224 (2005).

- [113] I. O. Troyanchuk, V. A. Khomchenko, H. Szymczak, and M. Baran, *J. Exp. Theor. Phys.* **97**, 1231 (2003).
- [114] T. Elovaara, H. Huhtinen, S. Majumdar, and P. Paturi, *Appl. Surf. Sci.* **381**, 17 (2016).

*Annales Universitatis Turkuensis*



Turun yliopisto  
University of Turku

ISBN 978-951-29-6872-5 (PRINT)  
ISBN 978-951-29-6873-2 (PDF)  
ISSN 0082-7002 (Print) | ISSN 2343-3175 (Online)